Research Square

Preprints are preliminary reports that have not undergone peer review.
They should not be considered conclusive, used to inform clinical practice,
or referenced by the media as validated information.

Mode competition in multimode flutter of a triple-tower suspension bridge

Wei Cui

State Key Lab of Disaster Reduction in Civil Engineering, Tongji University

Lin Zhao

zhaolin@tongji.edu.cn

Tongji University

Research Article

Keywords:

Posted Date: November 24th, 2026

DOI: https://doi.org/10.21203/rs.3.rs-11526145/v1

License: This work is licensed under a Creative Commons Attribution 4.0 International License.
Read Full License

Additional Declarations: No competing interests reported.

Mode competition in multimode flutter of a triple-tower suspension bridge

Wei Cui[1,2] and Lin Zhao[2,3*]

[1]State Key Lab of Disaster Reduction in Civil Engineering, Tongji University, Shanghai, 200092, China.
[2]Department of Bridge Engineering, College of Civil Engineering, Tongji University, Shanghai, 200092, China.
[3]Department of Bridge Engineering, College of Civil Engineering and Architecture, Guangxi University, Nanning, Guangxi, 530004, China.

*Corresponding author(s). E-mail(s): zhaolin@tongji.edu.cn;
Contributing authors: cuiwei@tongji.edu.cn;

Abstract

This study develops a four-mode model to investigate nonlinear flutter response selection in a triple-tower suspension bridge. First, the aerodynamic interactions are derived according to bridge symmetry while retaining the distinct symmetric and antisymmetric vertical–torsional frequencies. The amplitude and phase evolution equations are then obtained by complexification averaging. For the Maanshan Bridge inputs, the antisymmetric and symmetric flutter onset speeds are 71.9 and 88.7 m/s, respectively. The separate-pair calculations give the same thresholds, but the coupled baseline remains dominated by the antisymmetric response above the second onset. By introducing selective amplitude-dependent damping, the response selection can be changed. At 94 m/s, an assumed, uncalibrated dimensionless nonlinear damping coefficient of 120 reduces the antisymmetric normalized torsional amplitude by 88.33% relative to the undamped pure response, while the symmetric response accounts for 75.6% of the total normalized torsional amplitude. The amplitude-and-phase analysis shows that this mixed response is locally orbitally stable in the averaged model. The late-time responses agree closely with matched integrations of the original equations. The proposed formulation relates flutter onset to nonlinear response selection and identifies selective dissipation as a candidate mechanism for the experimentally reported suppression of antisymmetric motion.

Keywords: Long-span bridge, nonlinear flutter, multimode flutter, complexification averaging, mode competition, nonlinear damping

1 Introduction

A triple-tower suspension bridge consists of two main spans supported by three towers and is used for crossings over wide waterways or valleys [1]. By introducing a middle tower to support the adjacent spans, the main-span length can be reduced compared with a single-span suspension arrangement. The Taizhou Yangtze River Bridge in China has a span layout of (390+2×1080+390) m, which accommodates the wide crossing while maintaining navigation clearance.

Flutter can cause destructive wind-induced vibration of the bridge deck, as demonstrated by the collapse of the Tacoma Narrows Bridge [2]. For a triple-tower suspension bridge, the interaction between the two main spans affects the flutter characteristics [3]. At small amplitudes, the motion-induced lift and moment can be expressed through deck displacement and velocity using flutter derivatives [4]. Based on airfoil flutter theory [5], this linear aerodynamic formulation is widely used to calculate the flutter onset. When the wind speed exceeds the onset speed, however, the linear model predicts continuous amplitude growth and cannot determine the finite-amplitude response. As the deck motion increases, the aerodynamic force can change [6], and the response may develop into a sustained finite-amplitude limit-cycle oscillation [7], with higher harmonics in the aerodynamic force [8]. Therefore, nonlinear aerodynamic modeling is required to estimate the flutter response above onset.

The nonlinear aerodynamic force is often expressed by a polynomial expansion with frequency-dependent coefficients [9]. The coefficients can be determined by two main approaches. In quasi-steady theory [10], the force is obtained from static measurements at different angles of attack, and the deck motion is included through the effective angle of attack. Higher-order terms account for the force variation at increasing amplitudes, but the unsteady aerodynamic effects are neglected. Alternatively, the measured aerodynamic force of a vibrating deck can be fitted by a bivariate polynomial expansion [11]. The nonlinear coefficients are then identified from free-vibration [12] or forced-vibration tests [13].

For a triple-tower suspension bridge, the nonlinear flutter analysis should determine both the finite-amplitude limit-cycle oscillation (LCO) and the dominant vibration pattern of the two main spans. Traditionally, multimode flutter is analyzed using linear aerodynamics [14–16], while recent studies have considered the nonlinear response [17, 18]. The structural modes and flutter modes have different meanings in this analysis. A flutter response may contain two or more structural modes, such as vertical bending and torsion. The amplitude ratios and phase differences between these structural modes depend on the structural properties and aerodynamic forces.

More than one flutter mode can become unstable as the wind speed increases. For the symmetric and antisymmetric flutter responses, the vibration patterns differ on the two sides of the middle tower. The linear flutter analysis gives the onset speed of each response, but their interaction at appreciable amplitudes cannot be determined from the onset calculation. When both responses develop, the nonlinear aerodynamic force can limit their amplitudes and change the growth of one response through the other.

The interaction between symmetric and antisymmetric flutter can change the vibration distribution across the two spans. Therefore, the response above each onset speed should also be considered in the flutter assessment. In the full-bridge aeroelastic tests reported by Zhang and co-workers, the antisymmetric flutter at lower wind speeds changed to a symmetric response at higher wind speeds [19, 20]. Before this transition, the antisymmetric amplitude increased only slowly with wind speed. In this study, suppression refers to this slow amplitude growth between the initial onset and the transition. The transition was subsequently reproduced by a discrete model with structural nonlinearity [21] and a deep-learning-based full-bridge model [22].

This study develops a four-mode flutter model based on the bridge properties and the reported wind-tunnel response. Previous approaches include amplitude-dependent flutter derivatives [17], structural or geometric nonlinearity [18, 21], and deep-learning full-bridge simulations [22]. The present formulation retains the separate frequencies of the symmetric

and antisymmetric vertical–torsional responses and derives their aerodynamic interaction according to bridge symmetry. First, the nonlinear deck forces are projected onto the four structural modes. The evolution equations of the slowly varying amplitudes and relative phases are then derived by averaging. On the basis of these equations, the coexistence and local stability of the two flutter responses can be evaluated after both onset speeds have been exceeded. Amplitude-dependent damping is introduced selectively as a candidate mechanism for regulating the antisymmetric amplitude. Its effect on the existence and local stability of the combined response is examined together with the nonlinear aerodynamic interaction.

2 Bridge properties and measured flutter response

The Maanshan Yangtze River Bridge is located in Maanshan, Anhui Province, eastern China. The bridge has three towers and two main spans of 1080 m each. The middle tower is 128 m above the deck, while the side towers are 143 m above the deck and 176 m in overall height. Figure 2 shows the streamlined closed-box steel deck, which is 38.5 m wide and 3.5 m high. The stiffening girder is rigidly connected to the middle tower, and the main cables are continuous across it [23]. The tower–girder connection and cable continuity affect the coupled vibration of the two main spans.

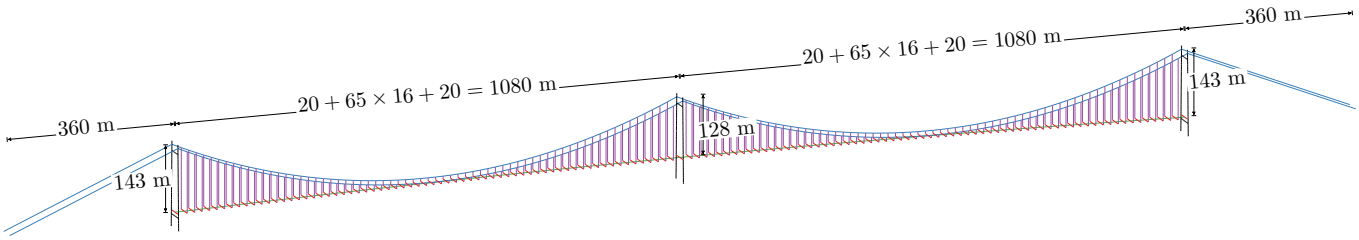

Fig. 1: Bridge layout and finite element model of the Maanshan Bridge

Figure 1 shows the finite element model established in ANSYS to calculate the vibration frequencies and mode shapes for the flutter analysis. The suspension cables and hangers,

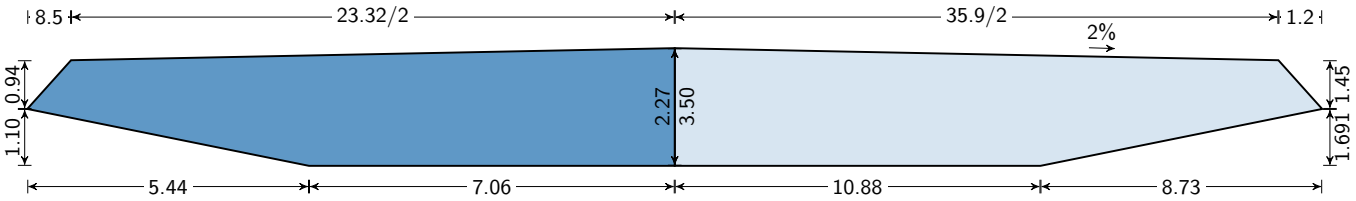

Fig. 2: Geometry of the bridge deck section (left: model scale, unit: cm; right: full scale, unit: m)

shown by the red and blue lines, respectively, are modeled using tension link elements (LINK180). The main girder, shown by the black lines, is modeled using beam elements (BEAM188) and connected to the hangers through a rigid "fish-bone" framework [24]. The nodes along the girder and suspension cables are located at the hanger attachment points.

Table 1: Vertical and torsional dynamic characteristics calculated by the ANSYS model

Mode	Frequency (Hz)	Modal Mass
AV1	0.0836	29322.4 (kg/m)
SV1	0.1167	28610.8 (kg/m)
AT1	0.2662	4793670 (kg·m^2/m)
ST1	0.3365	4657680 (kg·m^2/m)

The frequencies and modal masses of the vertical and torsional modes in Figure 3 are listed in Table 1. The antisymmetric flutter consists of the AV1 vertical-bending mode and the AT1 torsional mode. However, the ST1 torsional mode cannot couple with SV1 to form the corresponding symmetric flutter response. Although SV1 is symmetric about the middle tower, the vertical deformation within each main span is antisymmetric. The ST1 mode is symmetric both about the middle tower and within each span. Therefore, the different spanwise symmetries prevent aerodynamic coupling between SV1 and ST1 in the model.

In order to represent the symmetric flutter, a vertical response shape compatible with the symmetric torsion is required. With the girder fixed to the middle tower and the cables continuous across it, the first vertical-bending responses of the equal main spans are expressed as symmetric and antisymmetric combinations of the same span-bending shape. The ANSYS

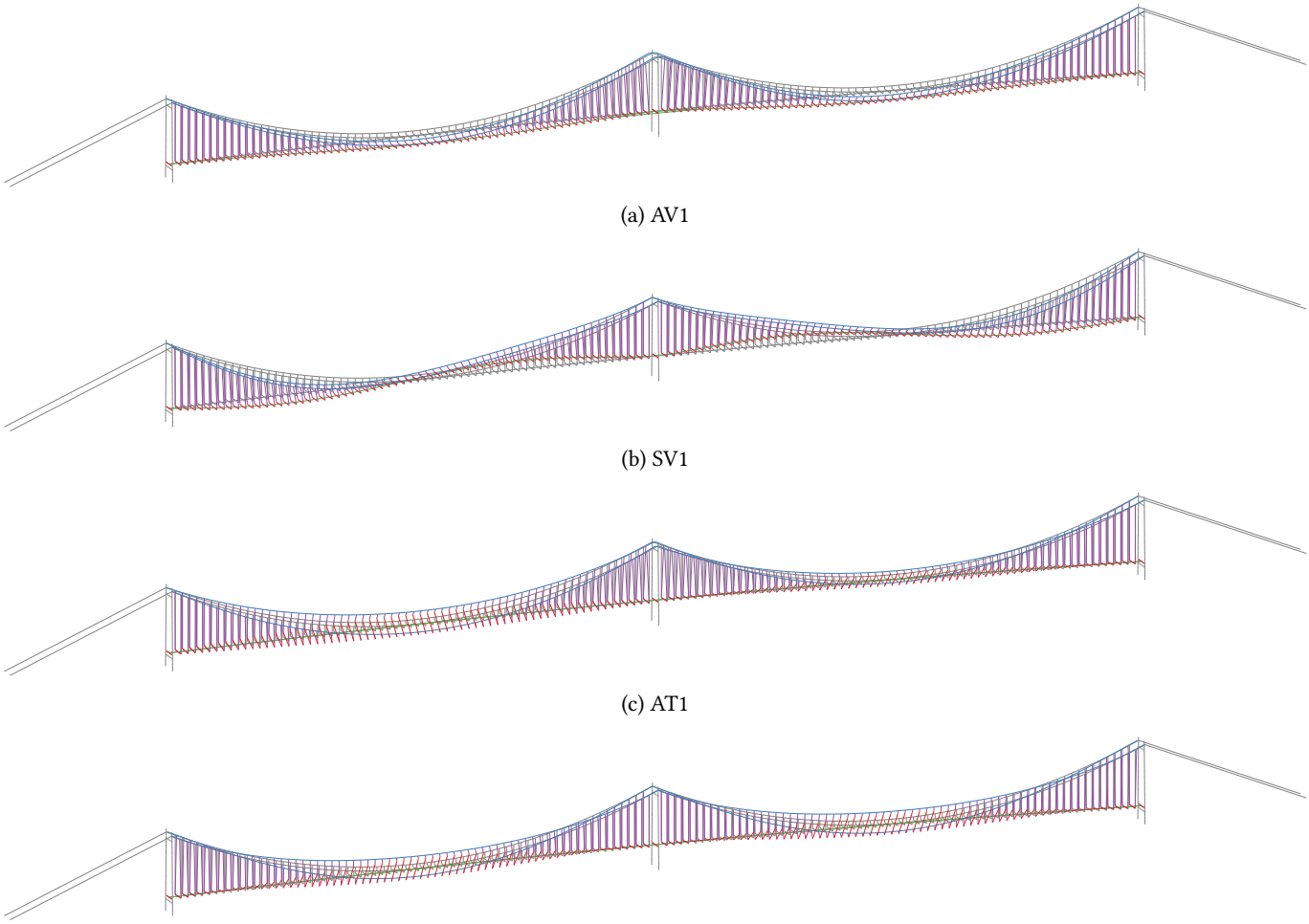

(a) AV1

(b) SV1

(c) AT1

(d) ST1

Fig. 3: Vertical and torsional mode shapes of the Maanshan Bridge finite element model (A: antisymmetric; S: symmetric; V: vertical bending; T: torsion; 1: first mode of each type)

mode sequence does not provide a first-order symmetric vertical-bending mode with the required symmetry within each span. Therefore, the symmetric counterpart of AV1 is constructed for the reduced model. The longitudinal bending stiffness of the middle tower is low compared with the effective vertical stiffness of the main-span system. By neglecting the tower contribution to the restoring force, the symmetric and antisymmetric vertical responses are assigned the same natural frequency in the reduced model.

A full-bridge aeroelastic model was tested in the TJ-3 wind tunnel at the State Key Laboratory for Disaster Reduction in Civil Engineering, Tongji University, China. The geometric scale was 1:211, and the frequency scale was 14.5258:1. The antisymmetric flutter onset speed obtained from the sectional model tests was 76.3 m/s, which was consistent with the full-bridge aeroelastic test. When the wind speed exceeded the onset speed, the antisymmetric amplitude increased only slowly. At 90.2 m/s, the flutter response changed to the symmetric pattern [19, 20]. Therefore, the nonlinear flutter model should examine both the limited antisymmetric amplitude growth after the first onset and the subsequent transition of the vibration pattern.

3 Reduced-order model for multimode flutter response

3.1 Governing equations and nonlinear aerodynamic forces

The governing equation of the bridge response under aerodynamic forces is

$$\boldsymbol{M}\boldsymbol{d}'' + \boldsymbol{C}\boldsymbol{d}' + \boldsymbol{K}\boldsymbol{d} = \boldsymbol{F}(\boldsymbol{d}, \boldsymbol{d}'; U) \tag{1}$$

where $\boldsymbol{d}$ is the deck displacement vector at spanwise coordinate x and dimensional time t. Its components are lateral displacement (sway) $p(x,t)$, vertical displacement (heave) $h(x,t)$, and rotation (pitch) $q(x,t)$, with $\boldsymbol{d} = \begin{bmatrix} p & h & q \end{bmatrix}^T$. The superscript T denotes transpose. The matrices $\boldsymbol{M}$, $\boldsymbol{C}$, and $\boldsymbol{K}$ are the mass, damping, and stiffness matrices, respectively, and $\boldsymbol{F}(\boldsymbol{d}, \boldsymbol{d}'; U)$ is the aerodynamic force at wind speed U. Primes denote differentiation with respect to t. Linear structural restoring forces are assumed in the baseline model, and nonlinear effects are included only in the aerodynamic forces.

The flutter response considered in this study consists of coupled vertical bending and torsion. Aerodynamic coupling occurs when the spanwise mode shapes have compatible symmetry (parity) and the corresponding projections of the distributed aerodynamic forces

are nonzero. The vertical and torsional equations of motion are

$$mh'' + c_h h' + k_h h = L_{se}(h', h, q', q; U) \tag{2a}$$

$$Iq'' + c_q q' + k_q q = M_{se}(h', h, q', q; U) \tag{2b}$$

where m and I are the deck mass and polar mass moment of inertia per unit span; c_h and c_q are the vertical and torsional damping coefficients per unit span; and k_h and k_q are the corresponding stiffness coefficients per unit span. The motion-induced lift L_{se} and pitching moment M_{se} are also defined per unit span.

Based on Scanlan's linear flutter model, the motion-induced lift and pitching moment can be expressed as

$$L_{\mathrm{se}} = \rho U^2 B \left(K H_1^* \frac{h'}{U} + K H_2^* \frac{B q'}{U} + K^2 H_3^* q + K^2 H_4^* \frac{h}{B} \right) \tag{3a}$$

$$M_{\mathrm{se}} = \rho U^2 B^2 \left(K A_1^* \frac{h'}{U} + K A_2^* \frac{B q'}{U} + K^2 A_3^* q + K^2 A_4^* \frac{h}{B} \right) \tag{3b}$$

where ρ is air density; U is the mean wind speed; $K = \omega B/U$ is the reduced frequency; B is the deck width; ω is the circular vibration frequency; and H_i^* and A_i^* ($i = 1 \sim 4$) are frequency-dependent flutter derivatives relating deck motion to lift and pitching moment.

The dimensionless vertical displacement and torsional rotation can be decomposed into the corresponding mode shapes and modal coordinates:

$$\frac{h(x,t)}{B} = \phi_y(x) y(t), \qquad q(x,t) = \phi_\theta(x)\theta(t). \tag{4}$$

Here the local rotation $q(x,t)$ is a dimensionless angle expressed in radians, $\theta(t)$ is the dimensionless torsional modal coordinate, and $\phi_\theta(x)$ is the torsional mode shape. The sectional rotation q and modal coordinate θ therefore represent different quantities. For a multimode response, the sectional rotation is obtained by summing the modal contributions.

Similarly, $y(t)$ is the dimensionless vertical modal coordinate, $\phi_y(x)$ is the vertical mode shape, and h/B is the dimensionless sectional vertical displacement.

By introducing the dimensionless time $\tau = tU/B$, the vertical and torsional equations of motion become

$$\ddot{y} + 2\xi_y K_y \dot{y} + K_y^2 y = \frac{m_y^*}{\phi_{yy}} \left(\phi_{yy} K H_1^* \dot{y} + \phi_{y\theta} K H_2^* \dot{\theta} + \phi_{y\theta} K^2 H_3^* \theta + \phi_{yy} K^2 H_4^* y \right) \tag{5a}$$

$$\ddot{\theta} + 2\xi_\theta K_\theta \dot{\theta} + K_\theta^2 \theta = \frac{m_\theta^*}{\phi_{\theta\theta}} \left(\phi_{y\theta} K A_1^* \dot{y} + \phi_{\theta\theta} K A_2^* \dot{\theta} + \phi_{\theta\theta} K^2 A_3^* \theta + \phi_{y\theta} K^2 A_4^* y \right) \tag{5b}$$

where ξ_y and ξ_θ are the structural damping ratios for vertical bending and torsion. The reduced structural frequencies are $K_y = \omega_y B/U$ and $K_\theta = \omega_\theta B/U$, where ω_y and ω_θ are the corresponding circular natural frequencies before aerodynamic coupling. A dot denotes differentiation with respect to τ. Accordingly, $\dot{q}$ and $\dot{\theta}$ are the derivatives of the sectional rotation and torsional modal coordinate, respectively, with respect to dimensionless time.

The aerodynamic forces in Eq. (3) are defined without a factor of $1/2$. The corresponding mass ratios are therefore $m_y^* = \rho B^2/m_y$ and $m_\theta^* = \rho B^4/I_\theta$, where m_y and I_θ are the uniform or effective sectional mass and polar inertia per unit span. The mode-shape weighting is introduced separately. For nonuniform sectional properties, the effective values can be calculated as $m_y = M_y/(L\phi_{yy})$ and $I_\theta = J_\theta/(L\phi_{\theta\theta})$, where M_y and J_θ are the generalized modal mass and inertia, and L is the deck length used in the modal integrals.

The aerodynamic weighting factors ϕ_{yy}, $\phi_{y\theta}$, and $\phi_{\theta\theta}$ are calculated from the spanwise mode shapes as $\phi_{yy} = \int_0^L \phi_y^2(x)\,dx/L$, $\phi_{y\theta} = \int_0^L \phi_y(x)\phi_\theta(x)\,dx/L$, and $\phi_{\theta\theta} = \int_0^L \phi_\theta^2(x)\,dx/L$. For symmetric bridge geometry and aerodynamic weighting, the linear coupling terms between modes of opposite symmetry vanish. Modes of the same symmetry can be aerodynamically coupled even when their modal orders differ.

For large-amplitude flutter response, the nonlinear lift and pitching moment are added to the linear aerodynamic forces:

$$\ddot{y} + 2\xi_y K_y \dot{y} + K_y^2 y = \frac{m_y^*}{\phi_{yy}} \Big[\phi_{yy} K H_1^* \dot{y} + \phi_{y\theta} K H_2^* \dot{\theta} + \phi_{y\theta} K^2 H_3^* \theta + \phi_{yy} K^2 H_4^* y + Q_y^{\mathrm{NL}}(\theta, \dot{\theta}) \Big], \tag{6a}$$

$$\ddot{\theta} + 2\xi_\theta K_\theta \dot{\theta} + K_\theta^2 \theta = \frac{m_\theta^*}{\phi_{\theta\theta}} \Big[\phi_{y\theta} K A_1^* \dot{y} + \phi_{\theta\theta} K A_2^* \dot{\theta} + \phi_{\theta\theta} K^2 A_3^* \theta + \phi_{y\theta} K^2 A_4^* y + Q_\theta^{\mathrm{NM}}(\theta, \dot{\theta}) \Big]. \tag{6b}$$

where Q_y^{NL} and Q_θ^{NM} are the generalized nonlinear lift and moment, respectively. They are obtained by projecting the sectional aerodynamic forces onto the corresponding mode shapes and integrating along the span.

The aerodynamic model is established from forced-motion tests of a Maanshan Bridge sectional model with a length scale of 1:154 (Figure 4) in the TJ-7 wind tunnel. The aerodynamic forces under prescribed vibration were measured using the forced-motion equipment described in [13].

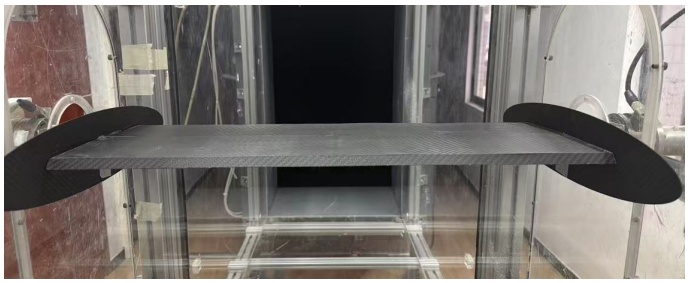

Fig. 4: Sectional model in the TJ-7 wind tunnel

The nonlinear aerodynamic terms were identified from the measured sectional forces using the method of Ma et al. [25].

For single-frequency sinusoidal motion, the reduced frequency is $K = \omega B/U$. Using sparse identification of nonlinear dynamics (SINDy), the dimensionless nonlinear sectional

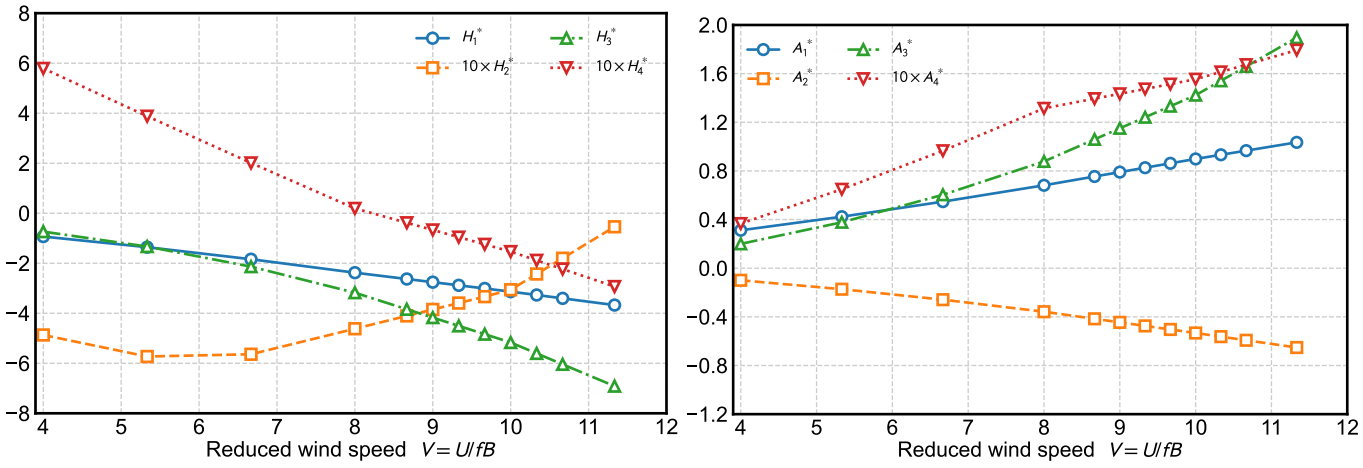

(a) H_1^*, H_2^*, H_3^*, and H_4^*

(b) A_1^*, A_2^*, A_3^*, and A_4^*

Fig. 5: Linear flutter derivatives of the bridge deck at different reduced wind speeds $V = U/(fB)$, where $f = \omega/(2\pi)$ is the vibration frequency in Hz and $V = 2\pi/K$.

forces are expressed in terms of the local rotation $q = q(x, \tau)$. The symbols n_L and n_M denote nonlinear lift and moment, and the superscripts (h) and (q) denote the contributions induced by heave and pitch, respectively. In the adopted model, the nonlinear aerodynamic terms depend on pitching motion, while the heave-only nonlinear contributions are set to zero:

$$n_L^{(h)}\left(\frac{h}{B}, \frac{\dot{h}}{B}\right) = 0, \tag{7a}$$

$$n_L^{(q)}(q, \dot{q}; K) = b_1 K^2 q\dot{q} + b_2 K^2 q(\dot{q})^2, \tag{7b}$$

$$n_M^{(h)}\left(\frac{h}{B}, \frac{\dot{h}}{B}\right) = 0, \tag{7c}$$

$$n_M^{(q)}(q, \dot{q}; K) = c_1 K(\dot{q})^2 + c_2 K^3 q^2 + c_3 K(\dot{q})^3. \tag{7d}$$

Here a dot on q denotes $dq/d\tau$, and a dot on θ denotes $d\theta/d\tau$. The coefficients $b_i = b_i(K)$ $(i = 1, 2)$ and $c_i = c_i(K)$ $(i = 1, 2, 3)$ are identified from the nonlinear lift and moment under single-frequency motion. Equation (7) therefore applies directly to single-frequency

response. When both flutter branches participate, their individual frequencies must be retained in the nonlinear interaction terms. The frequency-assignment rule for the receiving branch and source motion is introduced in Section 3.2.

The frequency-dependent coefficients $b_1(K)$, $b_2(K)$, $c_1(K)$, $c_2(K)$, and $c_3(K)$ identified from the tests are plotted in Figure 6.

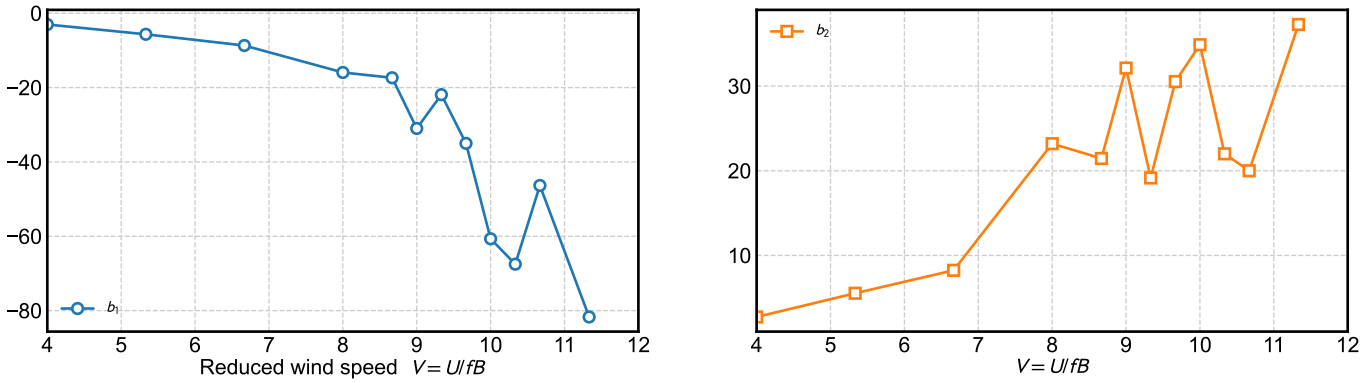

(a) b_1, b_2

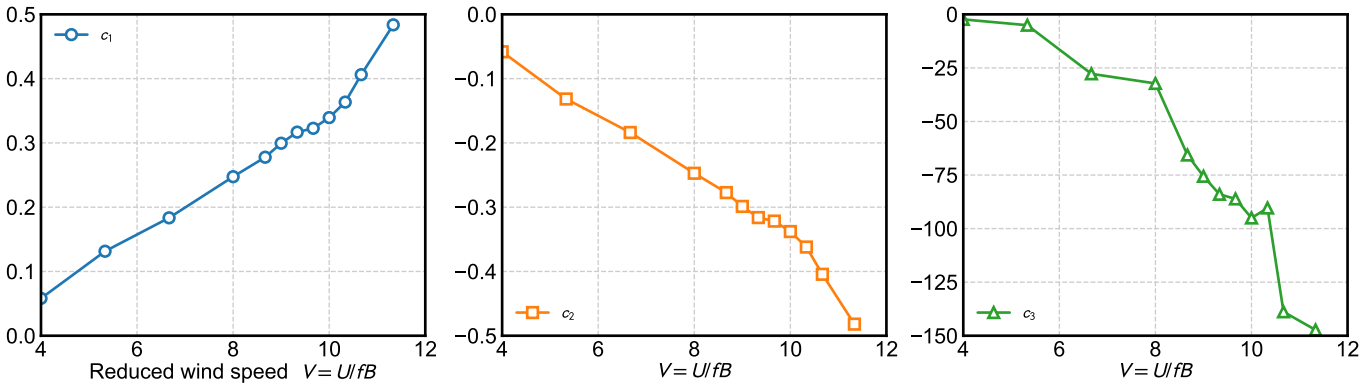

(b) c_1, c_2 and c_3

Fig. 6: Nonlinear aerodynamic coefficients of the bridge deck at different reduced wind speeds $V = U/(fB) = 2\pi/K$, where f is the vibration frequency in Hz.

By substituting the sectional rotation $q(x, \tau) = \phi_\theta(x)\theta(\tau)$ into the aerodynamic model and integrating along the span, the nonlinear vertical and torsional equations of motion are

obtained as

$$\ddot{y} + 2\xi_y K_y \dot{y} + K_y^2 y = \frac{m_y^*}{\phi_{yy}}[\phi_{yy} K H_1^* \dot{y} + \phi_{y\theta} K H_2^* \dot{\theta} + \phi_{y\theta} K^2 H_3^* \theta + \phi_{yy} K^2 H_4^* y + \phi_{\theta^2 y} b_1 K^2 \theta\dot{\theta} + \phi_{\theta^3 y} b_2 K^2 \theta\dot{\theta}^2] \tag{8a}$$

$$\ddot{\theta} + 2\xi_\theta K_\theta \dot{\theta} + K_\theta^2 \theta = \frac{m_\theta^*}{\phi_{\theta\theta}}[\phi_{y\theta} K A_1^* \dot{y} + \phi_{\theta\theta} K A_2^* \dot{\theta} + \phi_{\theta\theta} K^2 A_3^* \theta + \phi_{y\theta} K^2 A_4^* y + \phi_{\theta^3} c_1 K \dot{\theta}^2 + \phi_{\theta^3} c_2 K^3 \theta^2 + \phi_{\theta^4} c_3 K \dot{\theta}^3] \tag{8b}$$

where $\phi_{\theta^n y}$ and ϕ_{θ^n} are the modal weighting factors for the nonlinear sectional forces. The subscript θ denotes the torsional mode shape used in the projection, rather than the sectional rotation q. With n denoting the integer power of the torsional mode shape, the weighting factors are

$$\phi_{\theta^n y} = \frac{1}{L}\int_0^L \phi_y(x)\phi_\theta^n(x)\,dx, \qquad \phi_{\theta^n} = \frac{1}{L}\int_0^L \phi_\theta^n(x)\,dx. \tag{9}$$

3.2 Nonlinear aerodynamic coupling between two vertical–torsional mode pairs

When two vertical–torsional mode pairs are retained, the deck displacement is calculated by modal superposition. Let y_j and θ_j denote the dimensionless vertical and torsional modal coordinates, with corresponding mode shapes $\phi_{y_j}(x)$ and $\phi_{\theta_j}(x)$. The index $j = 1$ denotes the antisymmetric pair and $j = 2$ the symmetric pair. Then the sectional displacement and rotation are

$$h(x,\tau) = B\left[\phi_{y_1}(x)y_1(\tau) + \phi_{y_2}(x)y_2(\tau)\right] \tag{10a}$$

$$q(x,\tau) = \phi_{\theta_1}(x)\theta_1(\tau) + \phi_{\theta_2}(x)\theta_2(\tau) \tag{10b}$$

At a prescribed wind speed U, two aeroelastic flutter branches are tracked. Branch 1 consists of the coupled antisymmetric vertical and torsional modes, and branch 2 consists of the coupled symmetric modes. The remaining aeroelastic branches are assumed to retain

positive damping and are excluded from the retained flutter branches. Each retained branch has a reduced vibration frequency $K_j(U)$. The flutter onset speed is denoted by $U_{F,j}$, and the corresponding reduced frequency is $K_{F,j}$. The frequency used to evaluate the aerodynamic coefficients must be consistent with the coupled vibration frequency. Let $\lambda_j(K;U)$ denote the tracked dimensionless eigenvalue of branch j for the time variable $\tau = tU/B$. Then the frequency consistency and flutter onset conditions are

$$K_j(U) = \left|\operatorname{Im}\lambda_j(K_j(U);U)\right|, \qquad \operatorname{Re}\lambda_j(K_{F,j};U_{F,j}) = 0, \qquad K_{F,j} = K_j(U_{F,j}). \tag{11}$$

At linear flutter onset, the branch is neutrally stable. The same condition can be expressed in terms of the dynamic stiffness of the vertical–torsional pair with symmetry type j:

$$\det\left[-K_{F,j}^2\boldsymbol{I} + \imath K_{F,j}\left\{\boldsymbol{C}_{s,j} - \boldsymbol{C}_{a,j}(K_{F,j};U_{F,j})\right\} + \boldsymbol{D}_{s,j} - \boldsymbol{D}_{a,j}(K_{F,j};U_{F,j})\right] = 0. \tag{12}$$

where $\boldsymbol{I}$ is the identity matrix and $\imath^2 = -1$. The matrices $\boldsymbol{C}_{s,j}$ and $\boldsymbol{D}_{s,j}$ are the structural damping and stiffness matrices after division by modal mass, while $\boldsymbol{C}_{a,j}$ and $\boldsymbol{D}_{a,j}$ are the corresponding linear aerodynamic matrices. Each matrix is a two-coordinate block for pair j, and the complete matrices are given in Section 4.1. The operators Re and Im denote real and imaginary parts. Under the assumed bridge symmetry, the antisymmetric and symmetric pairs are uncoupled in the linear aerodynamic model. Their vibration frequencies can therefore be calculated separately. At the first wind-speed point, the higher positive-frequency eigen-pair in each block is used to initialize the torsional reduced frequency. As wind speed increases, the modal assurance criterion (MAC) is used to track each branch by comparison with the eigenvector at the preceding speed. This reference eigenvector is held fixed during the frequency iteration at the new speed. For an independent numerical check, the empirical frequency-order rule assigns the third and fourth modal frequencies of the complete four-coordinate system to branches 1 and 2, respectively. These selections agree with the

tracked branches over the investigated wind-speed range. The reduced structural frequencies $K_{y_j} = \omega_{y_j} B/U$ and $K_{\theta_j} = \omega_{\theta_j} B/U$ are calculated from the vertical and torsional circular natural frequencies ω_{y_j} and ω_{θ_j} before aerodynamic coupling. They are distinct from the coupled flutter frequency K_j and cannot be substituted for it. When U is sufficiently high for both retained flutter branches to participate, both reduced frequencies $K_1(U)$ and $K_2(U)$ are included in the initial response.

To extend the sectional aerodynamic model in Eq. (7) to the two-frequency response, the torsional motion is first decomposed into two modal contributions:

$$\begin{aligned} q_j(x,\tau) &= \phi_{\theta_j}(x)\theta_j(\tau), \qquad \dot{q}_j(x,\tau) = \phi_{\theta_j}(x)\dot{\theta}_j(\tau), \\ q(x,\tau) &= \sum_{j=1}^{2} q_j(x,\tau), \qquad \dot{q}(x,\tau) = \sum_{j=1}^{2} \dot{q}_j(x,\tau), \\ \mathcal{K}[q](x,\tau) &= \sum_{j=1}^{2} K_j q_j(x,\tau). \end{aligned} \tag{13}$$

where $\mathcal{K}$ is the operator that weights each modal contribution by its corresponding reduced frequency. Thus, $\mathcal{K}[q]$ is a frequency-weighted quantity rather than an additional displacement. The single-frequency tests identify the nonlinear forces for isolated motion. Mixed-frequency products such as $q_1\dot{q}_2$ or $q_1(\dot{q}_2)^2$ require an additional frequency-assignment assumption. The resulting interaction loads are not validated by the single-frequency measurements.

The adopted frequency assignment uses both the receiving mode pair and the source modal contributions. The effective nonlinear load for receiving branch $r \in \{1, 2\}$ is expressed as

$$\hat{n}^{\mathrm{NL}}_{L,r} = K_r \left[b_1^{(r)} \mathcal{K}[q]\dot{q} + b_2^{(r)} \mathcal{K}[q](\dot{q})^2 \right], \tag{14a}$$

$$\hat{n}^{\mathrm{NM}}_{M,r} = K_r \left[c_1^{(r)} (\dot{q})^2 + c_2^{(r)} \big(\mathcal{K}[q]\big)^2 + c_3^{(r)} (\dot{q})^3 \right], \tag{14b}$$

where $b_\ell^{(r)} = b_\ell(K_r)\,(\ell = 1, 2)$ and $c_\ell^{(r)} = c_\ell(K_r)\,(\ell = 1, 2, 3)$. The superscript (r) denotes evaluation at the receiving branch frequency K_r. The hat denotes the effective load assigned to each branch; these expressions do not define separate physical sectional loads. The leading frequency factor and aerodynamic coefficients are evaluated at the frequency of receiving branch r. Each displacement contribution q_j is weighted by its source frequency K_j through $\mathcal{K}[q]$. The velocities $\dot{q}_j$ are the exact derivatives with respect to τ, and their frequency dependence is introduced explicitly in the subsequent narrow-band representation. A comparison with an alternative frequency assignment is given in Appendix B.

The generalized aerodynamic forces are obtained by projection onto the receiving mode shape. The corresponding spanwise modal integrals are

$$\begin{aligned}
\phi_{\theta_{j_1}\cdots\theta_{j_p}y_r} &= \frac{1}{L}\int_0^L \phi_{y_r}(x)\prod_{a=1}^{p}\phi_{\theta_{j_a}}(x)\,dx,\\
\phi_{\theta_r\theta_{j_1}\cdots\theta_{j_p}} &= \frac{1}{L}\int_0^L \phi_{\theta_r}(x)\prod_{a=1}^{p}\phi_{\theta_{j_a}}(x)\,dx, \qquad j_a, r \in \{1, 2\}.
\end{aligned} \tag{15}$$

where p is the number of source-mode factors in the product, and j_a denotes the source branch of factor a. Repeated modal indices are expressed as powers; for example, $\phi_{\theta_1\theta_1 y_1} = \phi_{\theta_1^2 y_1}$. By substituting Eq. (13) into Eq. (14) and integrating along the span, the generalized nonlinear forces are obtained as

$$\mathcal{Q}_{y_r}^{\mathrm{NL}} = b_1^{(r)}K_r\sum_{j,k=1}^{2}K_j\phi_{\theta_j\theta_k y_r}\theta_j\dot{\theta}_k + b_2^{(r)}K_r\sum_{j,k,l=1}^{2}K_j\phi_{\theta_j\theta_k\theta_l y_r}\theta_j\dot{\theta}_k\dot{\theta}_l, \tag{16a}$$

$$\begin{aligned}
\mathcal{Q}_{\theta_r}^{\mathrm{NM}} = {} & c_1^{(r)}K_r\sum_{j,k=1}^{2}\phi_{\theta_r\theta_j\theta_k}\dot{\theta}_j\dot{\theta}_k\\
& + c_2^{(r)}K_r\sum_{j,k=1}^{2}K_jK_k\phi_{\theta_r\theta_j\theta_k}\theta_j\theta_k\\
& + c_3^{(r)}K_r\sum_{j,k,l=1}^{2}\phi_{\theta_r\theta_j\theta_k\theta_l}\dot{\theta}_j\dot{\theta}_k\dot{\theta}_l.
\end{aligned} \tag{16b}$$

The factors 2 and 3 in the expanded equations arise from repeated modal products. Before applying the bridge symmetry conditions, the b_1 term in the y_1 equation can be expanded as

$$\mathcal{Q}^{\mathrm{NL}}_{y_1,b_1} = b_1^{(1)} K_1 \left[K_1 \phi_{\theta_1^2 y_1} \theta_1 \dot{\theta}_1 + K_1 \phi_{\theta_1 \theta_2 y_1} \theta_1 \dot{\theta}_2 + K_2 \phi_{\theta_1 \theta_2 y_1} \theta_2 \dot{\theta}_1 + K_2 \phi_{\theta_2^2 y_1} \theta_2 \dot{\theta}_2 \right].$$

When only branch r is active, the generalized nonlinear forces reduce to

$$\begin{aligned} \mathcal{Q}^{\mathrm{NL}}_{y_r} &= \phi_{\theta_r^2 y_r} b_1(K_r) K_r^2 \theta_r \dot{\theta}_r + \phi_{\theta_r^3 y_r} b_2(K_r) K_r^2 \theta_r \dot{\theta}_r^2, \\ \mathcal{Q}^{\mathrm{NM}}_{\theta_r} &= \phi_{\theta_r^3} \left[c_1(K_r) K_r \dot{\theta}_r^2 + c_2(K_r) K_r^3 \theta_r^2 \right] + \phi_{\theta_r^4} c_3(K_r) K_r \dot{\theta}_r^3. \end{aligned}$$

The single-frequency generalized forces are therefore recovered. This formulation assumes a narrow-band response concentrated around the two retained flutter branch frequencies.

By substituting the generalized forces in Eq. (16) into the structural equations, the coupled equations of motion can be obtained. Each linear aerodynamic term is evaluated at the reduced frequency of its source motion. For the nonlinear terms, the receiving branch determines $b_\ell^{(r)}$, $c_\ell^{(r)}$, and the leading factor K_r, while each displacement contribution retains its corresponding source frequency K_j.

The complete four-mode equations before applying bridge symmetry are given in Appendix A.1. By applying the symmetry conditions, the equations reduce to Eq. (17). In Eq. (17), (y_1, θ_1) are the antisymmetric (odd) pair and (y_2, θ_2) are the symmetric (even) pair about midspan. The spanwise modal integrals are defined in Eq. (15), and the term-by-term complexification is given in Appendix A.2. For a bridge symmetric about midspan with symmetric (here uniform) aerodynamic weighting, the following modal integrals vanish: $\phi_{y_1 y_2}$, $\phi_{\theta_1 \theta_2}$, $\phi_{\theta_2 y_1}$, $\phi_{\theta_1 y_2}$, $\phi_{\theta_1^2 y_1}$, $\phi_{\theta_2^2 y_1}$, $\phi_{\theta_1 \theta_2 y_2}$, $\phi_{\theta_1^2 \theta_2 y_1}$, $\phi_{\theta_2^3 y_1}$, $\phi_{\theta_1^3 y_2}$, $\phi_{\theta_1 \theta_2^2 y_2}$, $\phi_{\theta_1^3}$, $\phi_{\theta_1 \theta_2^2}$, $\phi_{\theta_1^3 \theta_2}$, and $\phi_{\theta_1 \theta_2^3}$. These cancellations depend on the stated symmetry conditions and cannot be obtained from linear modal orthogonality alone. The structural mode shapes give diagonal mass and stiffness matrices. Classical damping is also assumed, so that the damping matrix

is diagonal in modal coordinates. Under exact bridge mode symmetry, the two mode pairs are linearly uncoupled. Therefore, the common reduced frequency K_j is used for all linear aerodynamic terms of pair (y_j, θ_j), and the nonlinear coefficients are $b_\ell^{(j)} = b_\ell(K_j)$ and $c_\ell^{(j)} = c_\ell(K_j)$. Using the aerodynamic force convention without a factor of $1/2$, the mass ratios for each pair are $m_{y_j}^* = \rho B^2/m_{y_j}$ and $m_{\theta_j}^* = \rho B^4/I_{\theta_j}$, with the effective sectional normalization defined above. The quantities m_{y_j} and I_{θ_j} are the effective mass and polar inertia per unit span for pair j, and ξ_{y_j} and ξ_{θ_j} are its structural damping ratios.

Then the coupled vertical and torsional equations of motion under the stated symmetry conditions are

$$\begin{aligned}\ddot{y}_1 + 2\xi_{y_1}K_{y_1}\dot{y}_1 + K_{y_1}^2 y_1 = \frac{m_{y_1}^*}{\phi_{y_1y_1}}[&\phi_{y_1y_1}K_1H_1^*(K_1)\dot{y}_1 + \phi_{y_1\theta_1}K_1H_2^*(K_1)\dot{\theta}_1 + \phi_{y_1\theta_1}K_1^2H_3^*(K_1)\theta_1 + \phi_{y_1y_1}K_1^2H_4^*(K_1)y_1 + \\ &\phi_{\theta_1\theta_2y_1}b_1^{(1)}\left(K_1^2\theta_1\dot{\theta}_2 + K_1K_2\theta_2\dot{\theta}_1\right) + \phi_{\theta_1^3y_1}b_2^{(1)}K_1^2\theta_1\dot{\theta}_1^2 + \\ &2\phi_{\theta_1\theta_2^2y_1}b_2^{(1)}K_1K_2\theta_2\dot{\theta}_1\dot{\theta}_2 + \phi_{\theta_1\theta_2^2y_1}b_2^{(1)}K_1^2\theta_1\dot{\theta}_2^2]\end{aligned} \tag{17a}$$

$$\begin{aligned}\ddot{y}_2 + 2\xi_{y_2}K_{y_2}\dot{y}_2 + K_{y_2}^2 y_2 = \frac{m_{y_2}^*}{\phi_{y_2y_2}}[&\phi_{y_2y_2}K_2H_1^*(K_2)\dot{y}_2 + \phi_{y_2\theta_2}K_2H_2^*(K_2)\dot{\theta}_2 + \phi_{y_2\theta_2}K_2^2H_3^*(K_2)\theta_2 + \phi_{y_2y_2}K_2^2H_4^*(K_2)y_2 + \\ &\phi_{\theta_1^2y_2}b_1^{(2)}K_1K_2\theta_1\dot{\theta}_1 + \phi_{\theta_2^2y_2}b_1^{(2)}K_2^2\theta_2\dot{\theta}_2 + \\ &\phi_{\theta_1^2\theta_2y_2}b_2^{(2)}K_2^2\theta_2\dot{\theta}_1^2 + 2\phi_{\theta_1^2\theta_2y_2}b_2^{(2)}K_1K_2\theta_1\dot{\theta}_1\dot{\theta}_2 + \phi_{\theta_2^3y_2}b_2^{(2)}K_2^2\theta_2\dot{\theta}_2^2]\end{aligned} \tag{17b}$$

$$\begin{aligned}\ddot{\theta}_1 + 2\xi_{\theta_1}K_{\theta_1}\dot{\theta}_1 + K_{\theta_1}^2\theta_1 = \frac{m_{\theta_1}^*}{\phi_{\theta_1\theta_1}}[&\phi_{y_1\theta_1}K_1A_1^*(K_1)\dot{y}_1 + \phi_{\theta_1\theta_1}K_1A_2^*(K_1)\dot{\theta}_1 + \phi_{\theta_1\theta_1}K_1^2A_3^*(K_1)\theta_1 + \phi_{y_1\theta_1}K_1^2A_4^*(K_1)y_1 + \\ &2\phi_{\theta_1^2\theta_2}c_1^{(1)}K_1\dot{\theta}_1\dot{\theta}_2 + 2\phi_{\theta_1^2\theta_2}c_2^{(1)}K_1^2K_2\theta_1\theta_2 + \\ &\phi_{\theta_1^4}c_3^{(1)}K_1\dot{\theta}_1^3 + 3\phi_{\theta_1^2\theta_2^2}c_3^{(1)}K_1\dot{\theta}_1\dot{\theta}_2^2]\end{aligned} \tag{17c}$$

$$\ddot{\theta}_2 + 2\xi_{\theta_2} K_{\theta_2} \dot{\theta}_2 + K_{\theta_2}^2 \theta_2 = \frac{m^*_{\theta_2}}{\phi_{\theta_2\theta_2}} [\phi_{y_2\theta_2} K_2 A_1^*(K_2)\dot{y}_2 + \phi_{\theta_2\theta_2} K_2 A_2^*(K_2)\dot{\theta}_2 + \phi_{\theta_2\theta_2} K_2^2 A_3^*(K_2)\theta_2 + \phi_{y_2\theta_2} K_2^2 A_4^*(K_2) y_2 +$$
$$\phi_{\theta_1^2\theta_2} c_1^{(2)} K_2 \dot{\theta}_1^2 + \phi_{\theta_2^3} c_1^{(2)} K_2 \dot{\theta}_2^2 + \phi_{\theta_1^2\theta_2} c_2^{(2)} K_1^2 K_2 \theta_1^2 + \phi_{\theta_2^3} c_2^{(2)} K_2^3 \theta_2^2 +$$
$$3\phi_{\theta_1^2\theta_2^2} c_3^{(2)} K_2 \dot{\theta}_1^2 \dot{\theta}_2 + \phi_{\theta_2^4} c_3^{(2)} K_2 \dot{\theta}_2^3] \tag{17d}$$

3.3 Flutter response evolution by complexification averaging

The amplitude growth or decay, sustained vibration amplitude, and phase difference between vertical and torsional motion can be calculated by complexification averaging. The response is decomposed into the slow evolution of amplitude and phase and the fast oscillation at each branch frequency. To express Eq. (17a) and the other modal equations in complex form, the displacement and velocity are combined as $\psi_{y_1} = \dot{y}_1 + \imath K_1 y_1$, $\psi_{y_2} = \dot{y}_2 + \imath K_2 y_2$, $\psi_{\theta_1} = \dot{\theta}_1 + \imath K_1 \theta_1$, and $\psi_{\theta_2} = \dot{\theta}_2 + \imath K_2 \theta_2$, where $\imath^2 = -1$.

The two reduced frequencies are retained separately. The formal near-1 : 1 ordering used in the averaging procedure is specified in Appendix A.2. In the numerical application, the resulting two-frequency equations are used at finite detuning. From the second linear instability at approximately 88.7 m/s to 100 m/s, the relative frequency separation $|K_2 - K_1|/[(K_1 + K_2)/2]$ ranges from 0.2828 to 0.2852. The accuracy at finite detuning is assessed by matched integrations of the original and averaged equations over three 600-cycle response histories at 90, 94, and 100 m/s, as described in Section 5.1. In these validation histories, the median active rate of amplitude and phase evolution, normalized by the corresponding reduced frequency, is 0.00372–0.00947.

For either coordinate $q_j \in \{y_j, \theta_j\}$ of pair $j = 1, 2$, the displacement, velocity, and acceleration can be written as

$$\begin{aligned} q_j &= \frac{\psi_{q_j} - \psi^*_{q_j}}{2\imath K_j}, \\ \dot{q}_j &= \frac{\psi_{q_j} + \psi^*_{q_j}}{2}, \\ \ddot{q}_j &= \dot{\psi}_{q_j} - \imath K_j \frac{\psi_{q_j} + \psi^*_{q_j}}{2}. \end{aligned} \tag{18}$$

Here the superscript $*$ denotes complex conjugation.

By substituting Eq. (18) into Eq. (17), the four equations of motion are rewritten in complex form as

$$\begin{aligned} &\dot{\psi}_{y_1} - \imath K_1 \frac{\psi_{y_1} + \psi^*_{y_1}}{2} + 2\xi_{y_1} K_{y_1} \frac{\psi_{y_1} + \psi^*_{y_1}}{2} + K^2_{y_1} \frac{\psi_{y_1} - \psi^*_{y_1}}{2\imath K_1} = K_1 \frac{m^*_{y_1}}{\phi_{y_1 y_1}} \Bigg[\\ &\quad \phi_{y_1 y_1} H^*_1(K_1) \frac{\psi_{y_1} + \psi^*_{y_1}}{2} + \phi_{y_1 \theta_1} H^*_2(K_1) \frac{\psi_{\theta_1} + \psi^*_{\theta_1}}{2} + \phi_{y_1 \theta_1} H^*_3(K_1) \frac{\psi_{\theta_1} - \psi^*_{\theta_1}}{2\imath} \\ &\quad + \phi_{y_1 y_1} H^*_4(K_1) \frac{\psi_{y_1} - \psi^*_{y_1}}{2\imath} + \phi_{\theta_1 \theta_2 y_1} b^{(1)}_1 \left(\frac{\psi_{\theta_1} - \psi^*_{\theta_1}}{2\imath} \frac{\psi_{\theta_2} + \psi^*_{\theta_2}}{2} + \frac{\psi_{\theta_2} - \psi^*_{\theta_2}}{2\imath} \frac{\psi_{\theta_1} + \psi^*_{\theta_1}}{2} \right) \\ &\quad + \phi_{\theta^3_1 y_1} b^{(1)}_2 \frac{\psi_{\theta_1} - \psi^*_{\theta_1}}{2\imath} \left(\frac{\psi_{\theta_1} + \psi^*_{\theta_1}}{2} \right)^2 + \phi_{\theta_1 \theta^2_2 y_1} b^{(1)}_2 \frac{\psi_{\theta_2} - \psi^*_{\theta_2}}{\imath} \frac{\psi_{\theta_1} + \psi^*_{\theta_1}}{2} \frac{\psi_{\theta_2} + \psi^*_{\theta_2}}{2} \\ &\quad + \phi_{\theta_1 \theta^2_2 y_1} b^{(1)}_2 \frac{\psi_{\theta_1} - \psi^*_{\theta_1}}{2\imath} \left(\frac{\psi_{\theta_2} + \psi^*_{\theta_2}}{2} \right)^2 \Bigg]. \end{aligned} \tag{19a}$$

$$\dot{\psi}_{y_2} - \iota K_2 \frac{\psi_{y_2} + \psi^*_{y_2}}{2} + 2\xi_{y_2} K_{y_2} \frac{\psi_{y_2} + \psi^*_{y_2}}{2} + K_{y_2}^2 \frac{\psi_{y_2} - \psi^*_{y_2}}{2\iota K_2} = K_2 \frac{m^*_{y_2}}{\phi_{y_2 y_2}} \Bigg[$$
$$\phi_{y_2 y_2} H_1^*(K_2) \frac{\psi_{y_2} + \psi^*_{y_2}}{2} + \phi_{y_2 \theta_2} H_2^*(K_2) \frac{\psi_{\theta_2} + \psi^*_{\theta_2}}{2} + \phi_{y_2 \theta_2} H_3^*(K_2) \frac{\psi_{\theta_2} - \psi^*_{\theta_2}}{2\iota}$$
$$+ \phi_{y_2 y_2} H_4^*(K_2) \frac{\psi_{y_2} - \psi^*_{y_2}}{2\iota} + \phi_{\theta_1^2 y_2} b_1^{(2)} \frac{\psi_{\theta_1} - \psi^*_{\theta_1}}{2\iota} \frac{\psi_{\theta_1} + \psi^*_{\theta_1}}{2} + \phi_{\theta_2^2 y_2} b_1^{(2)} \frac{\psi_{\theta_2} - \psi^*_{\theta_2}}{2\iota} \frac{\psi_{\theta_2} + \psi^*_{\theta_2}}{2} \tag{19b}$$
$$+ \phi_{\theta_1^2 \theta_2 y_2} b_2^{(2)} \frac{\psi_{\theta_2} - \psi^*_{\theta_2}}{2\iota} \left(\frac{\psi_{\theta_1} + \psi^*_{\theta_1}}{2} \right)^2$$
$$+ \phi_{\theta_1^2 \theta_2 y_2} b_2^{(2)} \frac{\psi_{\theta_1} - \psi^*_{\theta_1}}{\iota} \frac{\psi_{\theta_1} + \psi^*_{\theta_1}}{2} \frac{\psi_{\theta_2} + \psi^*_{\theta_2}}{2} + \phi_{\theta_2^3 y_2} b_2^{(2)} \frac{\psi_{\theta_2} - \psi^*_{\theta_2}}{2\iota} \left(\frac{\psi_{\theta_2} + \psi^*_{\theta_2}}{2} \right)^2 \Bigg].$$

$$\dot{\psi}_{\theta_1} - \iota K_1 \frac{\psi_{\theta_1} + \psi^*_{\theta_1}}{2} + 2\xi_{\theta_1} K_{\theta_1} \frac{\psi_{\theta_1} + \psi^*_{\theta_1}}{2} + K_{\theta_1}^2 \frac{\psi_{\theta_1} - \psi^*_{\theta_1}}{2\iota K_1} = K_1 \frac{m^*_{\theta_1}}{\phi_{\theta_1 \theta_1}} \Bigg[$$
$$\phi_{y_1 \theta_1} A_1^*(K_1) \frac{\psi_{y_1} + \psi^*_{y_1}}{2} + \phi_{\theta_1 \theta_1} A_2^*(K_1) \frac{\psi_{\theta_1} + \psi^*_{\theta_1}}{2} + \phi_{\theta_1 \theta_1} A_3^*(K_1) \frac{\psi_{\theta_1} - \psi^*_{\theta_1}}{2\iota}$$
$$+ \phi_{y_1 \theta_1} A_4^*(K_1) \frac{\psi_{y_1} - \psi^*_{y_1}}{2\iota} + 2\phi_{\theta_1^2 \theta_2} c_1^{(1)} \frac{\psi_{\theta_1} + \psi^*_{\theta_1}}{2} \frac{\psi_{\theta_2} + \psi^*_{\theta_2}}{2} \tag{19c}$$
$$+ 2\phi_{\theta_1^2 \theta_2} c_2^{(1)} \frac{\psi_{\theta_1} - \psi^*_{\theta_1}}{2\iota} \frac{\psi_{\theta_2} - \psi^*_{\theta_2}}{2\iota}$$
$$+ \phi_{\theta_1^4} c_3^{(1)} \left(\frac{\psi_{\theta_1} + \psi^*_{\theta_1}}{2} \right)^3 + 3\phi_{\theta_1^2 \theta_2^2} c_3^{(1)} \frac{\psi_{\theta_1} + \psi^*_{\theta_1}}{2} \left(\frac{\psi_{\theta_2} + \psi^*_{\theta_2}}{2} \right)^2 \Bigg].$$

$$\dot{\psi}_{\theta_2} - \iota K_2 \frac{\psi_{\theta_2} + \psi^*_{\theta_2}}{2} + 2\xi_{\theta_2} K_{\theta_2} \frac{\psi_{\theta_2} + \psi^*_{\theta_2}}{2} + K_{\theta_2}^2 \frac{\psi_{\theta_2} - \psi^*_{\theta_2}}{2\iota K_2} = K_2 \frac{m^*_{\theta_2}}{\phi_{\theta_2 \theta_2}} \Bigg[$$
$$\phi_{y_2 \theta_2} A_1^*(K_2) \frac{\psi_{y_2} + \psi^*_{y_2}}{2} + \phi_{\theta_2 \theta_2} A_2^*(K_2) \frac{\psi_{\theta_2} + \psi^*_{\theta_2}}{2} + \phi_{\theta_2 \theta_2} A_3^*(K_2) \frac{\psi_{\theta_2} - \psi^*_{\theta_2}}{2\iota}$$
$$+ \phi_{y_2 \theta_2} A_4^*(K_2) \frac{\psi_{y_2} - \psi^*_{y_2}}{2\iota} + \phi_{\theta_1^2 \theta_2} c_1^{(2)} \left(\frac{\psi_{\theta_1} + \psi^*_{\theta_1}}{2} \right)^2 + \phi_{\theta_2^3} c_1^{(2)} \left(\frac{\psi_{\theta_2} + \psi^*_{\theta_2}}{2} \right)^2 \tag{19d}$$
$$+ \phi_{\theta_1^2 \theta_2} c_2^{(2)} \left(\frac{\psi_{\theta_1} - \psi^*_{\theta_1}}{2\iota} \right)^2 + \phi_{\theta_2^3} c_2^{(2)} \left(\frac{\psi_{\theta_2} - \psi^*_{\theta_2}}{2\iota} \right)^2$$
$$+ 3\phi_{\theta_1^2 \theta_2^2} c_3^{(2)} \left(\frac{\psi_{\theta_1} + \psi^*_{\theta_1}}{2} \right)^2 \frac{\psi_{\theta_2} + \psi^*_{\theta_2}}{2} + \phi_{\theta_2^4} c_3^{(2)} \left(\frac{\psi_{\theta_2} + \psi^*_{\theta_2}}{2} \right)^3 \Bigg].$$

The complex variables are further decomposed as $\psi_{y_j} = \phi_{y_j} e^{\iota K_j \tau}$ and $\psi_{\theta_j} = \phi_{\theta_j} e^{\iota K_j \tau}$. The slow components describe the amplitude and phase evolution, and the exponential factors describe the fast oscillation at each branch frequency. Here $\phi_{y_j}(\tau)$ and $\phi_{\theta_j}(\tau)$ are the time-dependent complex response envelopes, distinct from the spatial mode shapes $\phi_{y_j}(x)$ and $\phi_{\theta_j}(x)$. The time argument of the envelopes is omitted below. Their polar forms are

$$\phi_{y_j} = A_{y_j} e^{\iota \beta_{y_j}}, \qquad A_{y_j} = |\phi_{y_j}|, \tag{20a}$$

$$\phi_{\theta_j} = A_{\theta_j} e^{\iota \beta_{\theta_j}}, \qquad A_{\theta_j} = |\phi_{\theta_j}|, \qquad j = 1, 2, \tag{20b}$$

where $A_{y_j}, A_{\theta_j} \geq 0$ are the envelope magnitudes, and β_{y_j} and β_{θ_j} are the slow phases. The corresponding dimensionless displacement amplitudes are A_{y_j}/K_j and A_{θ_j}/K_j. The harmonic expansion, removal of the fast branch-frequency factors, and term-by-term averaging are given in Appendix A.2.

By applying the averaging procedure in Appendix A.2, the evolution equations for the four complex modal envelopes are obtained as

$$\begin{aligned}
\dot{\phi}_{y_1} + \xi_{y_1} K_{y_1} \phi_{y_1} - \frac{\iota \left(K_{y_1}^2 - K_1^2\right)}{2K_1} \phi_{y_1} = K_1 \frac{m_{y_1}^*}{\phi_{y_1 y_1}} \Bigg[& \frac{\phi_{y_1 y_1}}{2} \left(H_1^*(K_1) - \iota H_4^*(K_1)\right) \phi_{y_1} \\
& + \frac{\phi_{y_1 \theta_1}}{2} \left(H_2^*(K_1) - \iota H_3^*(K_1)\right) \phi_{\theta_1} - \frac{\iota}{8} \phi_{\theta_1^3 y_1} b_2^{(1)} \phi_{\theta_1}^2 \phi_{\theta_1}^* \\
& - \frac{\iota}{8} \phi_{\theta_1 \theta_2^2 y_1} b_2^{(1)} \left(2 \phi_{\theta_1} \phi_{\theta_2} \phi_{\theta_2}^* + \phi_{\theta_1}^* \phi_{\theta_2}^2 e^{2\iota(K_2 - K_1)\tau}\right) \Bigg],
\end{aligned} \tag{21a}$$

$$\begin{aligned}
\dot{\phi}_{y_2} + \xi_{y_2} K_{y_2} \phi_{y_2} - \frac{\iota \left(K_{y_2}^2 - K_2^2\right)}{2K_2} \phi_{y_2} = K_2 \frac{m_{y_2}^*}{\phi_{y_2 y_2}} \Bigg[& \frac{\phi_{y_2 y_2}}{2} \left(H_1^*(K_2) - \iota H_4^*(K_2)\right) \phi_{y_2} \\
& + \frac{\phi_{y_2 \theta_2}}{2} \left(H_2^*(K_2) - \iota H_3^*(K_2)\right) \phi_{\theta_2} - \frac{\iota}{8} \phi_{\theta_2^3 y_2} b_2^{(2)} \phi_{\theta_2}^2 \phi_{\theta_2}^* \\
& - \frac{\iota}{8} \phi_{\theta_1^2 \theta_2 y_2} b_2^{(2)} \left(2 \phi_{\theta_1} \phi_{\theta_1}^* \phi_{\theta_2} + \phi_{\theta_1}^2 \phi_{\theta_2}^* e^{2\iota(K_1 - K_2)\tau}\right) \Bigg],
\end{aligned} \tag{21b}$$

$$\dot{\phi}_{\theta_1} + \xi_{\theta_1} K_{\theta_1} \phi_{\theta_1} - \frac{\iota\left(K_{\theta_1}^2 - K_1^2\right)}{2K_1}\phi_{\theta_1} = K_1 \frac{m^*_{\theta_1}}{\phi_{\theta_1\theta_1}}\Bigg[\frac{\phi_{y_1\theta_1}}{2}\left(A_1^*(K_1) - \iota A_4^*(K_1)\right)\phi_{y_1} + \frac{\phi_{\theta_1\theta_1}}{2}\left(A_2^*(K_1) - \iota A_3^*(K_1)\right)\phi_{\theta_1} + \frac{3}{8}\phi_{\theta_1^4} c_3^{(1)} \phi_{\theta_1}^2 \phi_{\theta_1}^* + \frac{3}{8}\phi_{\theta_1^2\theta_2^2} c_3^{(1)}\left(2\phi_{\theta_1}\phi_{\theta_2}\phi_{\theta_2}^* + \phi_{\theta_1}^*\phi_{\theta_2}^2 e^{2\iota(K_2-K_1)\tau}\right)\Bigg], \tag{21c}$$

$$\dot{\phi}_{\theta_2} + \xi_{\theta_2} K_{\theta_2} \phi_{\theta_2} - \frac{\iota\left(K_{\theta_2}^2 - K_2^2\right)}{2K_2}\phi_{\theta_2} = K_2 \frac{m^*_{\theta_2}}{\phi_{\theta_2\theta_2}}\Bigg[\frac{\phi_{y_2\theta_2}}{2}\left(A_1^*(K_2) - \iota A_4^*(K_2)\right)\phi_{y_2} + \frac{\phi_{\theta_2\theta_2}}{2}\left(A_2^*(K_2) - \iota A_3^*(K_2)\right)\phi_{\theta_2} + \frac{3}{8}\phi_{\theta_2^4} c_3^{(2)} \phi_{\theta_2}^2 \phi_{\theta_2}^* + \frac{3}{8}\phi_{\theta_1^2\theta_2^2} c_3^{(2)}\left(2\phi_{\theta_1}\phi_{\theta_1}^*\phi_{\theta_2} + \phi_{\theta_1}^2\phi_{\theta_2}^* e^{2\iota(K_1-K_2)\tau}\right)\Bigg]. \tag{21d}$$

The sustained response branches at different wind speeds are calculated using the time-independent part of Eq. (21), termed the autonomous secular subsystem. This subsystem excludes the oscillatory beat terms proportional to $e^{2\iota(K_2-K_1)\tau}$ and $e^{2\iota(K_1-K_2)\tau}$. The complete averaged equations and the autonomous secular subsystem are therefore distinguished in the comparison of response histories and the calculation of sustained amplitudes.

For comparison with the independent-pair approximation, the nonlinear interaction between θ_1 and θ_2 is removed by omitting the terms proportional to $\phi_{\theta_1\theta_2^2 y_1}$, $\phi_{\theta_1^2\theta_2 y_2}$, and $\phi_{\theta_1^2\theta_2^2}$. Then Eq. (21) reduces to two independent vertical–torsional pairs. The evolution equations for the antisymmetric pair (y_1, θ_1) are

$$\dot{\phi}_{y_1} + \xi_{y_1} K_{y_1} \phi_{y_1} - \frac{\iota\left(K_{y_1}^2 - K_1^2\right)}{2K_1}\phi_{y_1} = \frac{m^*_{y_1}}{\phi_{y_1 y_1}}\Bigg[\frac{\phi_{y_1 y_1} K_1}{2}\left(H_1^*(K_1) - \iota H_4^*(K_1)\right)\phi_{y_1} + \frac{\phi_{y_1\theta_1} K_1}{2}\left(H_2^*(K_1) - \iota H_3^*(K_1)\right)\phi_{\theta_1} - \frac{\iota K_1}{8}\phi_{\theta_1^3 y_1} b_2^{(1)} \phi_{\theta_1}^2 \phi_{\theta_1}^*\Bigg], \tag{22a}$$

$$\dot{\phi}_{\theta_1} + \xi_{\theta_1} K_{\theta_1} \phi_{\theta_1} - \frac{\iota\left(K_{\theta_1}^2 - K_1^2\right)}{2K_1}\phi_{\theta_1} = \frac{m_{\theta_1}^*}{\phi_{\theta_1\theta_1}}\left[\frac{\phi_{y_1\theta_1}K_1}{2}\left(A_1^*(K_1) - \iota A_4^*(K_1)\right)\phi_{y_1}\right.$$
$$\left. + \frac{\phi_{\theta_1\theta_1}K_1}{2}\left(A_2^*(K_1) - \iota A_3^*(K_1)\right)\phi_{\theta_1} + \frac{3K_1}{8}\phi_{\theta_1^4}c_3^{(1)}\phi_{\theta_1}^2\phi_{\theta_1}^*\right]. \tag{22b}$$

The response equations for the symmetric pair (y_2, θ_2) can be obtained by the same procedure. Each independent pair, (y_2, θ_2) or (y_1, θ_1), retains the vertical–torsional coupling within that pair and excludes the nonlinear interaction between the two pairs.

4 Flutter onset and nonlinear response estimation

4.1 Critical wind speeds from complex eigenvalue analysis

The critical wind speed, vibration frequency, amplitude ratio, and phase difference at flutter onset are evaluated by complex eigenvalue analysis. When the vibration amplitudes are small, the nonlinear terms can be neglected, and flutter onset is determined by the transition from decay to growth of the response.

Omitting the nonlinear terms in Eq. (17), the first-order state equation is written as

$$\dot{\boldsymbol{\chi}} = \boldsymbol{A}\boldsymbol{\chi} \tag{23}$$

where $\boldsymbol{\chi} = \left[y_1 \;\; \theta_1 \;\; y_2 \;\; \theta_2 \;\; \dot{y}_1 \;\; \dot{\theta}_1 \;\; \dot{y}_2 \;\; \dot{\theta}_2\right]^T$ is the displacement–velocity state vector, and $\boldsymbol{A} = \begin{bmatrix} \boldsymbol{O} & \boldsymbol{I} \\ -\boldsymbol{D} & -\boldsymbol{C} \end{bmatrix}$ is the state matrix in reduced time. The blocks $\boldsymbol{O}$ and $\boldsymbol{I}$ are the 4×4 zero and identity matrices. The effective stiffness $\boldsymbol{D}$ is $\boldsymbol{D} = \boldsymbol{D}_s - \boldsymbol{D}_a$, where $\boldsymbol{D}_s$ and $\boldsymbol{D}_a$ are the structural and aerodynamic stiffness matrices, respectively. The effective damping $\boldsymbol{C}$ is $\boldsymbol{C} = \boldsymbol{C}_s - \boldsymbol{C}_a$, where $\boldsymbol{C}_s$ and $\boldsymbol{C}_a$ are the structural and aerodynamic damping matrices. These matrices are expressed in modal coordinates with modal-mass normalization and reduced-time scaling.

With diag denoting a diagonal matrix, their expressions are

$$\boldsymbol{D}_s = \mathrm{diag}\left[K_{y_1}^2 \;\; K_{\theta_1}^2 \;\; K_{y_2}^2 \;\; K_{\theta_2}^2\right] \tag{24a}$$

$$\boldsymbol{C}_s = \mathrm{diag}\left[2K_{y_1}\xi_{y_1} \;\; 2K_{\theta_1}\xi_{\theta_1} \;\; 2K_{y_2}\xi_{y_2} \;\; 2K_{\theta_2}\xi_{\theta_2}\right] \tag{24b}$$

$$\boldsymbol{C}_a = \begin{bmatrix} m_{y_1}^* H_1^*(K_1)K_1 & \dfrac{\phi_{y_1\theta_1}}{\phi_{y_1y_1}} m_{y_1}^* H_2^*(K_1)K_1 & 0 & 0 \\ \dfrac{\phi_{y_1\theta_1}}{\phi_{\theta_1\theta_1}} m_{\theta_1}^* A_1^*(K_1)K_1 & m_{\theta_1}^* A_2^*(K_1)K_1 & 0 & 0 \\ 0 & 0 & m_{y_2}^* H_1^*(K_2)K_2 & \dfrac{\phi_{y_2\theta_2}}{\phi_{y_2y_2}} m_{y_2}^* H_2^*(K_2)K_2 \\ 0 & 0 & \dfrac{\phi_{y_2\theta_2}}{\phi_{\theta_2\theta_2}} m_{\theta_2}^* A_1^*(K_2)K_2 & m_{\theta_2}^* A_2^*(K_2)K_2 \end{bmatrix} \tag{24c}$$

$$\boldsymbol{D}_a = \begin{bmatrix} m_{y_1}^* H_4^*(K_1)K_1^2 & \dfrac{\phi_{y_1\theta_1}}{\phi_{y_1y_1}} m_{y_1}^* H_3^*(K_1)K_1^2 & 0 & 0 \\ \dfrac{\phi_{y_1\theta_1}}{\phi_{\theta_1\theta_1}} m_{\theta_1}^* A_4^*(K_1)K_1^2 & m_{\theta_1}^* A_3^*(K_1)K_1^2 & 0 & 0 \\ 0 & 0 & m_{y_2}^* H_4^*(K_2)K_2^2 & \dfrac{\phi_{y_2\theta_2}}{\phi_{y_2y_2}} m_{y_2}^* H_3^*(K_2)K_2^2 \\ 0 & 0 & \dfrac{\phi_{y_2\theta_2}}{\phi_{\theta_2\theta_2}} m_{\theta_2}^* A_4^*(K_2)K_2^2 & m_{\theta_2}^* A_3^*(K_2)K_2^2 \end{bmatrix} \tag{24d}$$

In $\boldsymbol{D}_a$, H_4^* and A_3^* represent the direct aerodynamic stiffness terms, whereas H_3^* and A_4^* represent the coupling between vertical displacement and deck rotation, consistent with Eq. (17).

For each eigenvalue λ of the dimensionless state matrix $\boldsymbol{A}$, the real part determines response growth or decay, and the magnitude of the imaginary part gives the reduced vibration frequency. Denoting the two parts by $\Re(\lambda)$ and $\Im(\lambda)$, respectively, a signed damping indicator is defined as

$$\hat{\zeta} = -\frac{\Re(\lambda)}{2|\Im(\lambda)|} \times 100\%. \tag{25}$$

When $\hat{\zeta} > 0$, the small-amplitude response decays; $\hat{\zeta} = 0$ gives flutter onset, and $\hat{\zeta} < 0$ indicates exponential growth. The normalization of this onset indicator differs from that of the conventional modal damping ratio, $\zeta_m = -\Re(\lambda)/|\lambda|$.

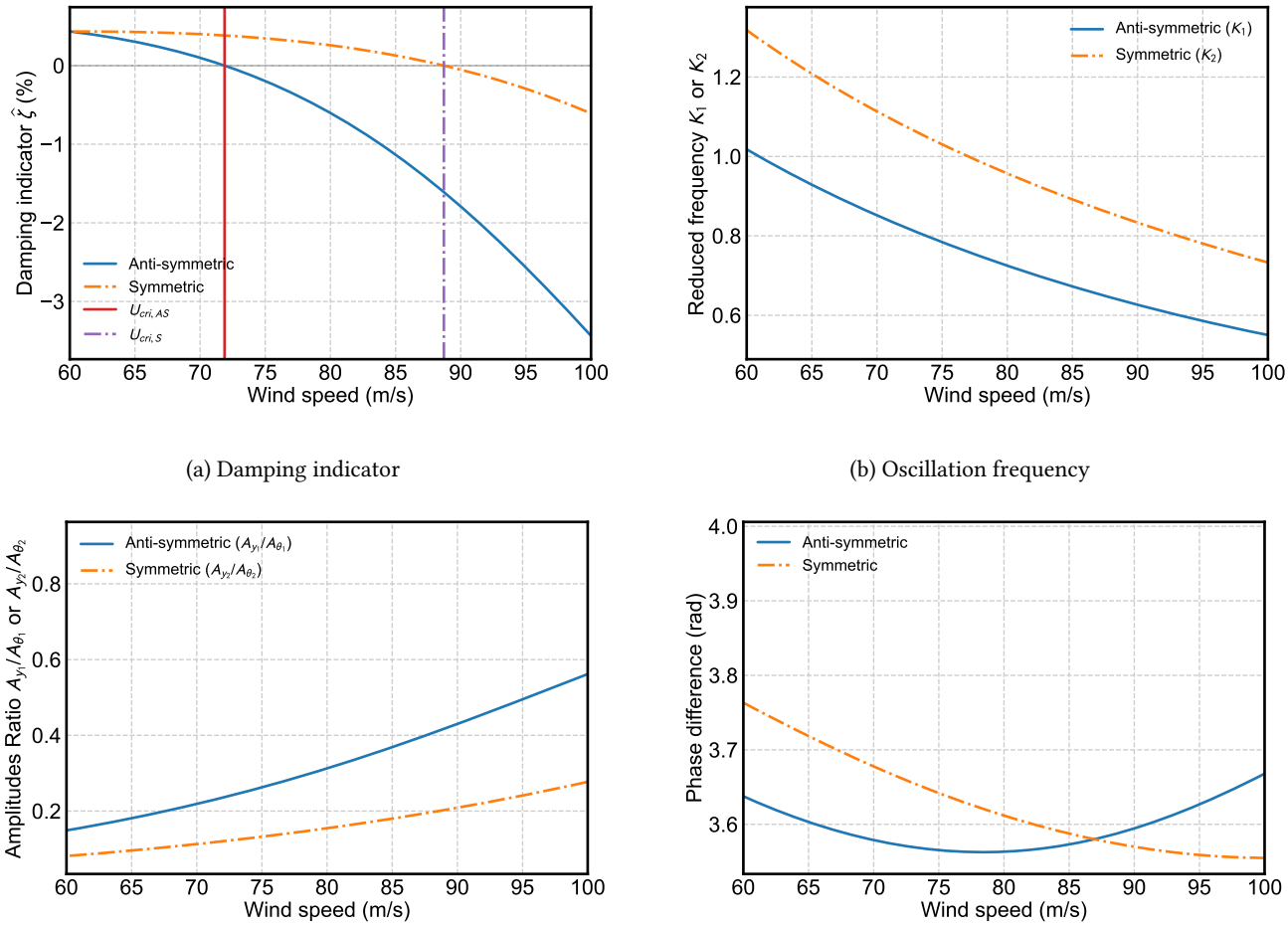

(a) Damping indicator

(b) Oscillation frequency

(c) Amplitude ratios between vertical and torsional motion

(d) Phase differences between vertical and torsional motion

Fig. 7: Linear flutter characteristics of the symmetric and antisymmetric vertical–torsional response patterns. In panel (c), A_{y_j}/A_{θ_j} is the vertical-to-torsional amplitude ratio of pair j, with $j = 1$ antisymmetric and $j = 2$ symmetric.

Figure 7a shows that the critical wind speed of the antisymmetric flutter mode (AT1) is 71.9 m/s, lower than 88.7 m/s for the symmetric flutter mode (ST1). Under the assumed bridge symmetry, the linearized equations separate into antisymmetric and symmetric vertical–torsional pairs. Therefore, the isolated-pair and four-mode calculations give the same onset thresholds. The reduced vibration frequencies at different wind speeds are plotted in Figure 7b. The wind-tunnel study reported antisymmetric flutter onset at 76.3 m/s and a transition from the existing flutter response to symmetric-dominated motion at 90.2 m/s [20]. The measured 90.2 m/s transition is a nonlinear response change, whereas the predicted 88.7 m/s threshold is the linear instability of the symmetric pair. Figures 7c and 7d plot the vertical–torsional amplitude ratios and phase differences. Above flutter onset, the amplitude ratio increases and the phase difference decreases for both response patterns.

4.2 Nonlinear flutter amplitudes and response evolution

The linear analysis determines flutter onset, whereas the sustained amplitudes and dominant response pattern depend on the nonlinear interaction. When the amplitudes increase, the nonlinear terms in Eqs. (14) and (17) affect the amplitude evolution. For the baseline cases examined here, these terms limit the response growth and produce a constant-amplitude limit-cycle oscillation.

The flutter responses at each wind speed are calculated by time integration of Eq. (17), using the two-frequency aerodynamic approximation in Eq. (14). The Runge–Kutta method uses a 5th-order solution and 4th-order error estimation. The initial torsional amplitude is 0.1° for both response patterns. The corresponding initial vertical displacements and velocities are determined from the amplitude ratios and phase differences in Figure 7.

Figure 8a plots the flutter response at $U = 84.25$ m/s, between the two onset speeds. The antisymmetric amplitudes increase to a limit-cycle oscillation (LCO). Since the wind speed is below the symmetric onset threshold, the amplitudes of y_2 and θ_2 decay. The sustained response is therefore dominated by one vertical–torsional pair, as in a conventional coupled-flutter calculation.

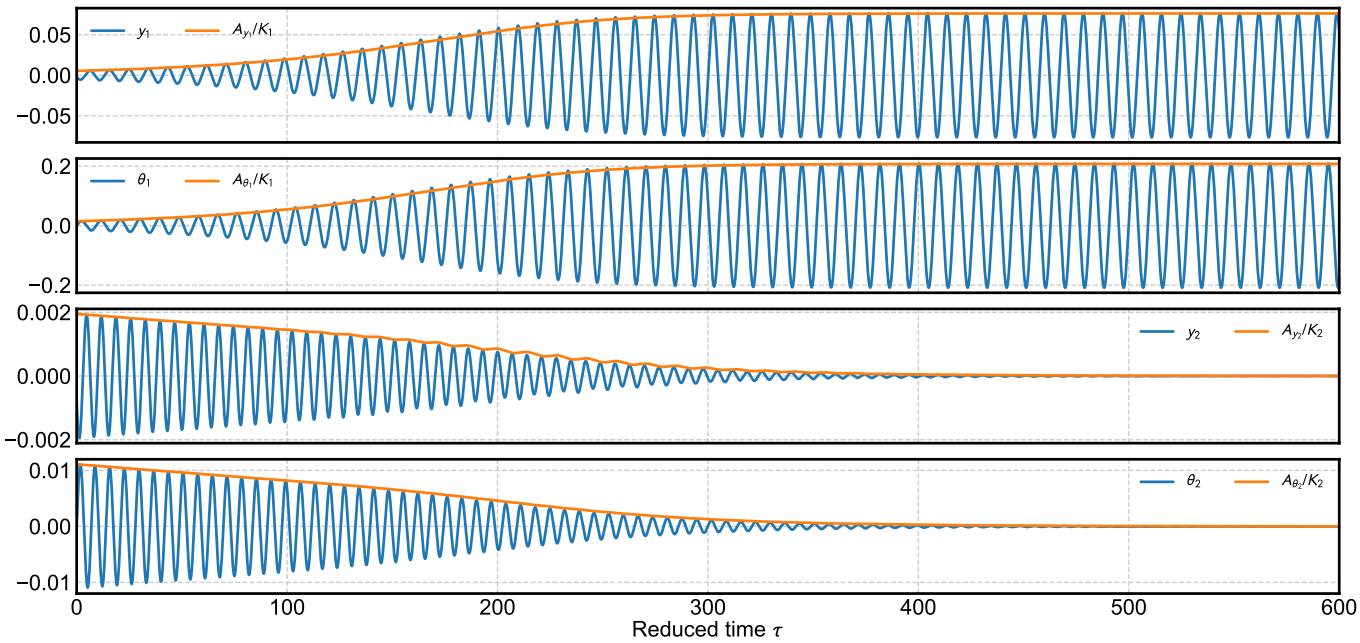

(a) $U = 84.25$ m/s, between the two linear instability thresholds.

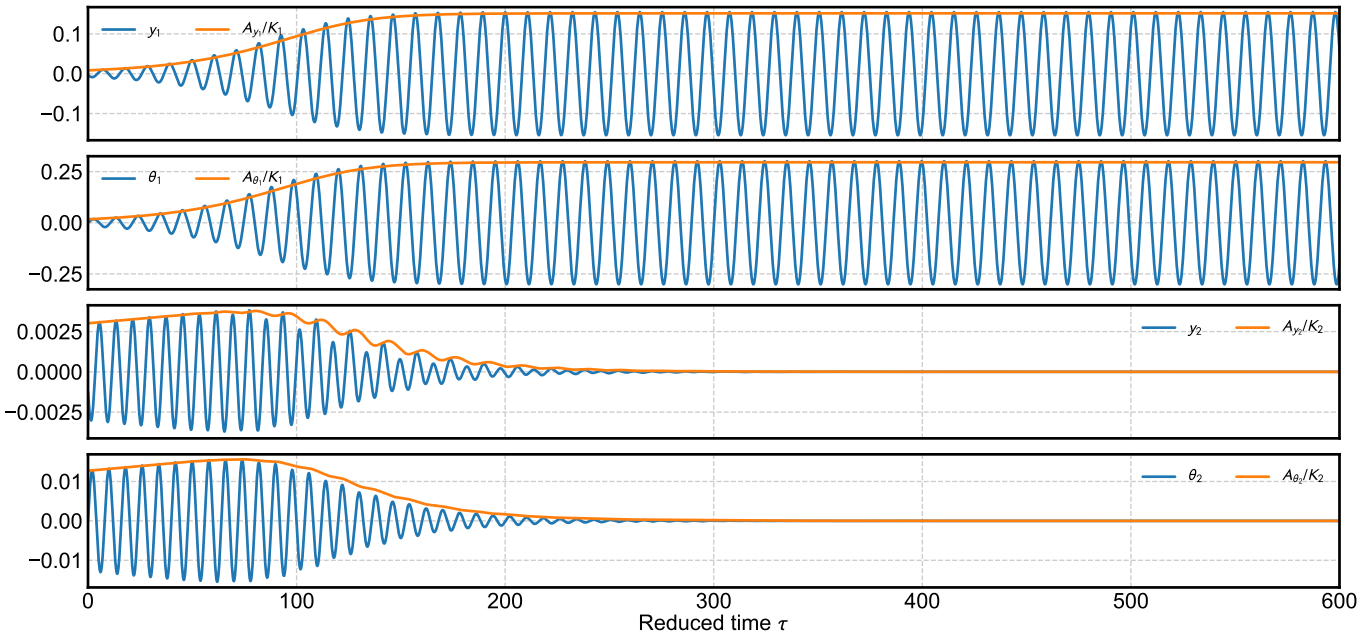

(b) $U = 94.42$ m/s, above the second linear instability threshold.

Fig. 8: Time histories of the coupled flutter response at $U = 84.25$ and 94.42 m/s.

Figure 8b shows the response at $U = 94.42$ m/s, where both response patterns are linearly unstable and their amplitudes initially increase. As the amplitudes develop, the symmetric response (y_2, θ_2) decays, while the antisymmetric response (y_1, θ_1) approaches a sustained oscillation. Therefore, a wind speed above the symmetric onset threshold does not ensure a sustained symmetric response. The nonlinear interaction changes the amplitude evolution and permits energy exchange between the two response patterns.

The sustained flutter amplitudes in Figure 9 are evaluated by solving the fixed-point equations for the time-independent part of Eq. (21). As specified in Section 3.3, the calculation omits the oscillatory terms proportional to $e^{2\iota(K_2-K_1)\tau}$ and $e^{2\iota(K_1-K_2)\tau}$. The envelope magnitudes and phases are defined in Eq. (20). Figure 9 reports the displacement amplitudes A_{y_j}/K_j and A_{θ_j}/K_j, as indicated in its legends, whereas Figure 10 uses $(A_{\theta_1}, A_{\theta_2})$ directly. For any active component, indexed here by $\nu \in \{y_1, \theta_1, y_2, \theta_2\}$,

$$\dot{\phi}_\nu = \left(\dot{A}_\nu + \iota A_\nu \dot{\beta}_\nu\right) e^{\iota\beta_\nu}. \tag{26}$$

When $A_\nu > 0$, the fixed-point condition $\dot{\phi}_\nu = 0$ requires constant amplitude and phase, $\dot{A}_\nu = \dot{\beta}_\nu = 0$. When $A_\nu = 0$, the phase is undefined, and only the amplitude condition applies. Grouping the four components into their vertical–torsional pairs gives

$$\begin{aligned} \boldsymbol{\phi} &= \begin{bmatrix} \boldsymbol{\phi}_1 \\ \boldsymbol{\phi}_2 \end{bmatrix}, \qquad \boldsymbol{\phi}_j = \begin{bmatrix} \phi_{y_j} \\ \phi_{\theta_j} \end{bmatrix}, \\ \dot{\boldsymbol{\phi}} &= \boldsymbol{f}(\boldsymbol{\phi}; U), \quad \boldsymbol{f} = \begin{bmatrix} \boldsymbol{f}_1 \\ \boldsymbol{f}_2 \end{bmatrix}, \qquad j = 1, 2. \end{aligned} \tag{27}$$

where $\boldsymbol{f}_j$ is the amplitude-and-phase evolution function of response pair $\boldsymbol{\phi}_j$, and $\boldsymbol{f}$ combines both pairs. At each wind speed, the reference frequencies $K_1(U)$ and $K_2(U)$ are fixed by Eq. (11). The constant complex response relative to these reference oscillations is denoted

by $\boldsymbol{\phi}^{\mathrm{fp}}$, where the superscript fp identifies a fixed point, satisfying

$$\boldsymbol{f}(\boldsymbol{\phi}^{\mathrm{fp}}; U) = \mathbf{0} \quad \Longleftrightarrow \quad \begin{bmatrix} \mathrm{Re}\, \boldsymbol{f} \\ \mathrm{Im}\, \boldsymbol{f} \end{bmatrix} = \mathbf{0}. \tag{28}$$

Equation (28) provides eight real equations for the real and imaginary parts of the four components of $\boldsymbol{\phi}^{\mathrm{fp}}$. Solving these equations gives the sustained flutter amplitudes $A_{y_j} = |\phi_{y_j}^{\mathrm{fp}}|$ and $A_{\theta_j} = |\phi_{\theta_j}^{\mathrm{fp}}|$, and the vertical–torsional phase difference of pair j is $\beta_{y_j} - \beta_{\theta_j}$. The common phase origin of an active pair sets the time reference without changing its amplitudes or vertical–torsional phase difference. The calculation for Figure 9 retains the reference frequencies without introducing an additional frequency correction.

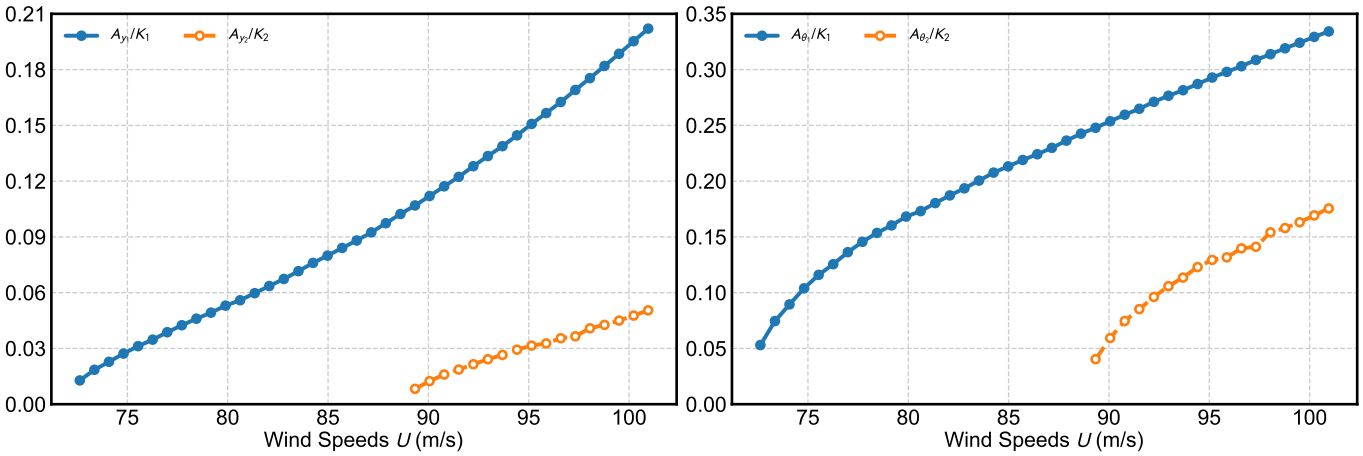

(a) Vertical amplitudes

(b) Torsional amplitudes

Fig. 9: Sustained vertical and torsional flutter amplitudes at different wind speeds.

Figure 9 plots the sustained flutter amplitudes over the displayed wind-speed range. The solid lines in Figure 9 show that the antisymmetric-dominated baseline response persists above the second onset speed. The dashed lines in Figure 9 are the symmetric amplitudes calculated from the isolated vertical–torsional pair, using the system described after Eq. (22).

The coupled baseline response examined here does not approach this isolated-pair prediction because the nonlinear interaction with the antisymmetric response suppresses the symmetric component. Thus, the isolated-pair calculation gives the onset speed but does not determine the sustained coupled response.

4.3 Evolution characteristics of torsional amplitudes

The torsional-amplitude evolution is evaluated at the two wind speeds in Figure 8. The arrows and streamlines represent the amplitude derivatives $(\dot{A}_{\theta_1}, \dot{A}_{\theta_2})$ at different combinations of $(A_{\theta_1}, A_{\theta_2})$. With the phase held fixed, the plots describe the amplitude evolution over the displayed range and its relation to the sustained antisymmetric response.

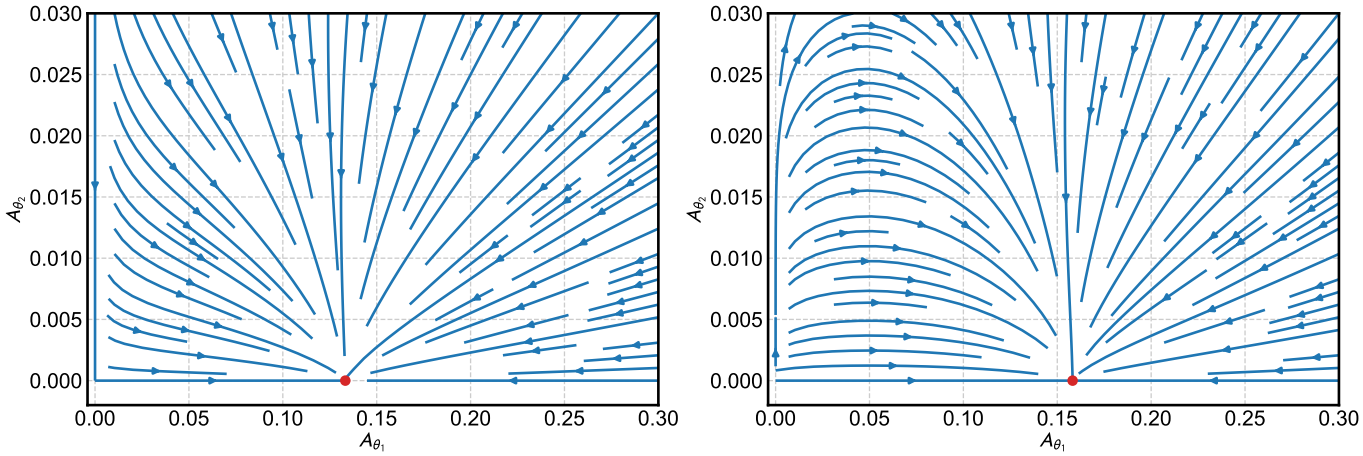

(a) $U = 84.25$ m/s

(b) $U = 94.42$ m/s

Fig. 10: Torsional-amplitude vector fields of the baseline model at $U = 84.25$ and 94.42 m/s, with phase held fixed. Filled circles mark sustained antisymmetric responses on the $A_{\theta_2} = 0$ axis.

When $U = 84.25$ m/s, between the two onset speeds, the symmetric amplitude decays throughout the displayed range. The streamlines approach the sustained antisymmetric response at $(A_{\theta_1}, A_{\theta_2}) = (0.13328, 0)$ (Figure 10a). When $U = 94.42$ m/s, the symmetric amplitude initially increases for some amplitude combinations. The streamlines then

approach the $A_{\theta_2} = 0$ axis and the sustained antisymmetric response at $(0.15816, 0)$ (Figure 10b). This amplitude evolution agrees with the time histories and shows that an initially growing component can decay in the subsequent nonlinear response.

The vector fields describe the baseline antisymmetric dominance for the selected phases and displayed amplitude range, consistent with the time histories.

5 Effect of hypothetic amplitude-dependent damping on response selection

Figures 8 and 9 show that the baseline model retains a sustained antisymmetric-dominated response above the symmetric linear-instability threshold. In the full-bridge test, the antisymmetric amplitude was limited, followed by rapid growth of the symmetric response [19, 20]. A cubic damping term is therefore introduced in the first torsional coordinate to investigate selective amplitude-dependent dissipation as a candidate mechanism for this response change. Equation (17c) becomes

$$\begin{aligned}\ddot{\theta}_1 + 2\xi_{\theta_1} K_{\theta_1} \dot{\theta}_1 + \xi_{\mathrm{nl}} \theta_1^2 \dot{\theta}_1 + K_{\theta_1}^2 \theta_1 = \frac{m^*_{\theta_1}}{\phi_{\theta_1\theta_1}} \Big[& \phi_{y_1\theta_1} K_1 A_1^*(K_1) \dot{y}_1 + \phi_{\theta_1\theta_1} K_1 A_2^*(K_1) \dot{\theta}_1 + \\ & \phi_{\theta_1\theta_1} K_1^2 A_3^*(K_1) \theta_1 + \phi_{y_1\theta_1} K_1^2 A_4^*(K_1) y_1 + 2\phi_{\theta_1^2\theta_2} c_1^{(1)} K_1 \dot{\theta}_1 \dot{\theta}_2 + 2\phi_{\theta_1^2\theta_2} c_2^{(1)} K_1^2 K_2 \theta_1 \theta_2 + \\ & \phi_{\theta_1^4} c_3^{(1)} K_1 \dot{\theta}_1^3 + 3\phi_{\theta_1^2\theta_2^2} c_3^{(1)} K_1 \dot{\theta}_1 \dot{\theta}_2^2 \Big].\end{aligned} \tag{29}$$

where $\xi_{\mathrm{nl}} > 0$ is the additional damping coefficient. The power contribution is $-\xi_{\mathrm{nl}} \theta_1^2 \dot{\theta}_1^2 \leq 0$, so this term is always dissipative. The dissipation acts directly on antisymmetric torsional motion and increases with its amplitude. Its effect on the symmetric response is transmitted through the interaction between the two response patterns.

Averaging the additional damping term in Eq. (29) gives the following contribution to Eq. (21), which reduces the growth of the antisymmetric torsional amplitude:

$$\dot{\phi}_{\theta_1}\Big|_{\mathrm{nl}} = -\frac{\xi_{\mathrm{nl}}}{8K_1^2}\phi_{\theta_1}^2\phi_{\theta_1}^*. \tag{30}$$

Since the reduced time $\tau = tU/B$ and deck rotation θ_1 are dimensionless, the damping coefficient is also dimensionless. This coefficient is an uncalibrated model parameter. The illustrative calculation uses $\xi_{\mathrm{nl}} = 120$, and the deterministic sensitivity analysis covers $0 \leq \xi_{\mathrm{nl}} \leq 240$.

The calculations are performed on the full wind-speed grid $U = 90, 91, \ldots, 100$ m/s or at the representative wind speeds $U = 90$, 94, and 100 m/s. Figure 11 compares the sustained amplitudes across the full grid. The additional damping selectively reduces the antisymmetric response within this model.

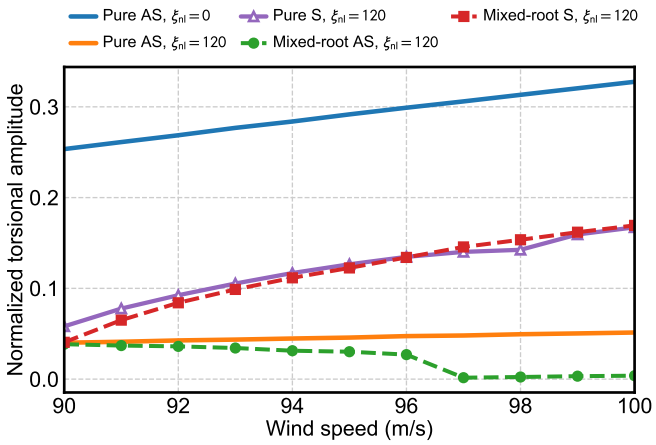

Fig. 11: Effect of the assumed amplitude-dependent damping on sustained normalized torsional flutter amplitudes. AS and S in the legend denote antisymmetric and symmetric motion.

When $U = 94$ m/s, the fixed-phase amplitude equilibrium changes from a pure antisymmetric response to a mixed response after the additional damping is introduced (Figure 14).

The two eigenvalues of its amplitude Jacobian are negative. The local orbital stability of this mixed response is evaluated below with both amplitude and phase variations included.

The amplitude-and-phase stability analysis allows the nonlinear response frequency to differ from the linear reference. Denote the reduced frequency of the sustained response of pair j by K_j^{nl} and its correction to the linear reference by $\Delta K_j = K_j^{\mathrm{nl}} - K_j$. A relative equilibrium has a constant complex modal vector $\boldsymbol{\phi}_j^{\mathrm{re}}$ and a common phase advancing at ΔK_j, where the superscript re denotes the relative equilibrium. Its governing equations are

$$\begin{aligned} \boldsymbol{\phi}_j(\tau) &= e^{\imath \Delta K_j \tau} \boldsymbol{\phi}_j^{\mathrm{re}}, \\ \boldsymbol{f}_j(\boldsymbol{\phi}^{\mathrm{re}}; U) - \imath \Delta K_j \boldsymbol{\phi}_j^{\mathrm{re}} &= \mathbf{0}, \qquad j = 1, 2. \end{aligned} \tag{31}$$

Each pair oscillates at K_j^{nl} with constant amplitudes and vertical–torsional phase difference. When $\Delta K_j = 0$, Eq. (31) reduces to the fixed-point condition in Eq. (28). One phase condition is imposed for each active pair to fix its arbitrary time reference.

Local orbital stability is determined from the decay or growth of small amplitude and relative-phase perturbations. The Jacobian of the averaged equations is evaluated in a frame rotating with the response. The neutral common-phase directions are removed because they only change the time reference. The remaining eigenvalues $\lambda_\perp$ determine the perturbation evolution. When their largest real part, $\max \mathrm{Re}\, \lambda_\perp$, is negative, all such small perturbations decay; a positive value indicates at least one growing perturbation. A negative value closer to zero corresponds to a slower local decay rate.

At $U = 94$ m/s and the assumed $\xi_{\mathrm{nl}} = 120$, the antisymmetric normalized torsional amplitude decreases by 88.33% relative to the undamped pure response. The symmetric share of the total normalized torsional amplitude, $A_{\theta_2}/(A_{\theta_1} + A_{\theta_2})$, is 0.756 (Table 3). The mixed response is locally orbitally stable in the averaged amplitude-and-phase system, whereas the pure antisymmetric and pure symmetric responses are unstable. This local stability of the computed mixed response is retained across the tested wind-speed grid. Therefore, selective damping can change the sustained flutter response within the model.

5.1 Validation of averaged flutter response estimation

The averaged flutter responses at $\xi_{\mathrm{nl}} = 120$ are compared with direct integration of the original four-mode equations. Identical inputs, initial conditions, and solver settings are used for both calculations. The amplitude envelopes, vibration frequencies, and vertical–torsional phase differences are evaluated at 90, 94, and 100 m/s over a common 600-cycle window.

Figure 12 compares the amplitude envelopes from the averaged equations with the original flutter response. Over these 600-cycle histories, the late-time envelopes, vibration frequencies, and vertical–torsional phase differences agree closely. The matched small perturbations decay in the original equations, supporting the predicted local recovery over the tested histories. The discrepancy in transient amplitude evolution increases toward the upper end of the tested wind-speed range.

5.2 Sensitivity to the assumed nonlinear damping

The damping-sensitivity analysis continues the mixed response over 21 damping levels ($\xi_{\mathrm{nl}} = 0, 12, \ldots, 240$) and 11 wind speeds ($U = 90, 91, \ldots, 100$ m/s), keeping all other inputs fixed. A solution is accepted as mixed when both vertical–torsional pairs remain active and the residual in the rotating frame is below 10^{-7}. Common-phase directions are removed before the local orbital stability is evaluated.

Figure 13 shows 200 computed mixed responses among 231 coarse-grid cases. All computed responses are locally orbitally stable in the averaged system, and the remaining cases are unresolved. As the additional damping increases, the computed mixed-response branch extends to lower wind speeds. In panel (a), blue and grey cells denote locally orbitally stable responses and unresolved calculations, respectively. The black line marks the lowest computed damping value reached by decreasing the coefficient in steps of 1.2. Panel (b) shows the symmetric torsional share, $A_{\theta_2}/(A_{\theta_1} + A_{\theta_2})$. Representative lowest computed damping

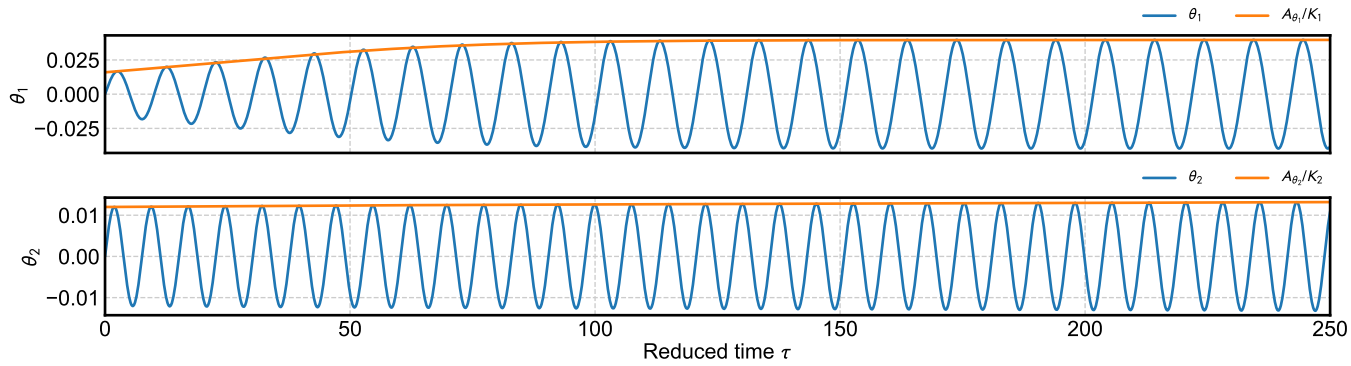

(a) $U = 90$ m/s, $0 \leq \tau \leq 250$.

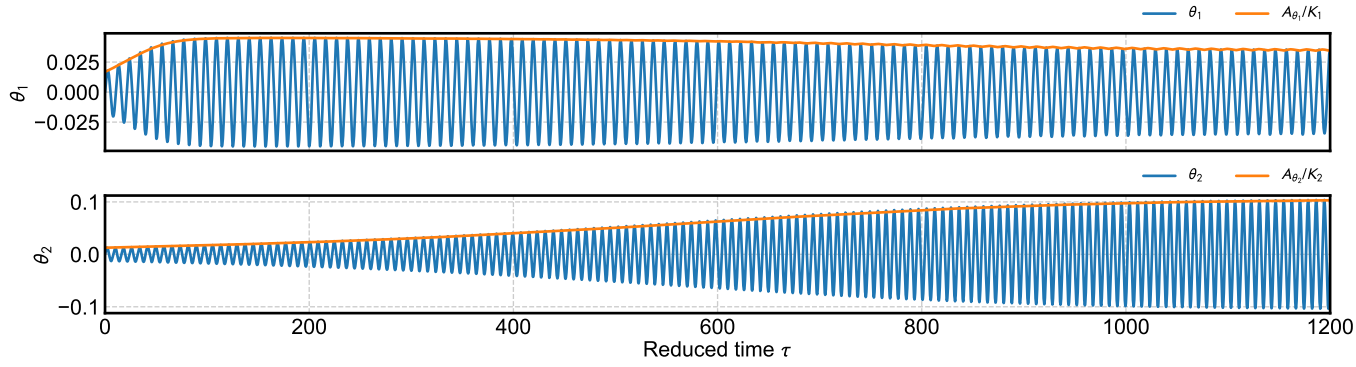

(b) $U = 94$ m/s, $0 \leq \tau \leq 1200$.

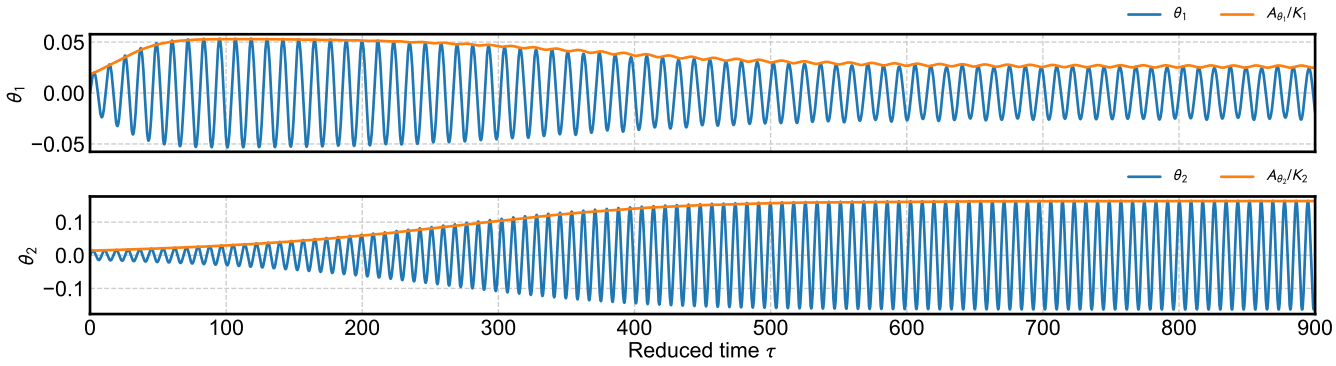

(c) $U = 100$ m/s, $0 \leq \tau \leq 900$.

Fig. 12: Comparison of torsional flutter histories from the original equations (blue) with amplitude envelopes from the averaged equations (orange)

values ($\xi_{\mathrm{nl}}^{\mathrm{found}}$) and adjacent lower unresolved values ($\xi_{\mathrm{nl}}^{\mathrm{unr}}$) are listed in Table 2. These values describe the limit of successful numerical continuation and do not establish the physical existence boundary.

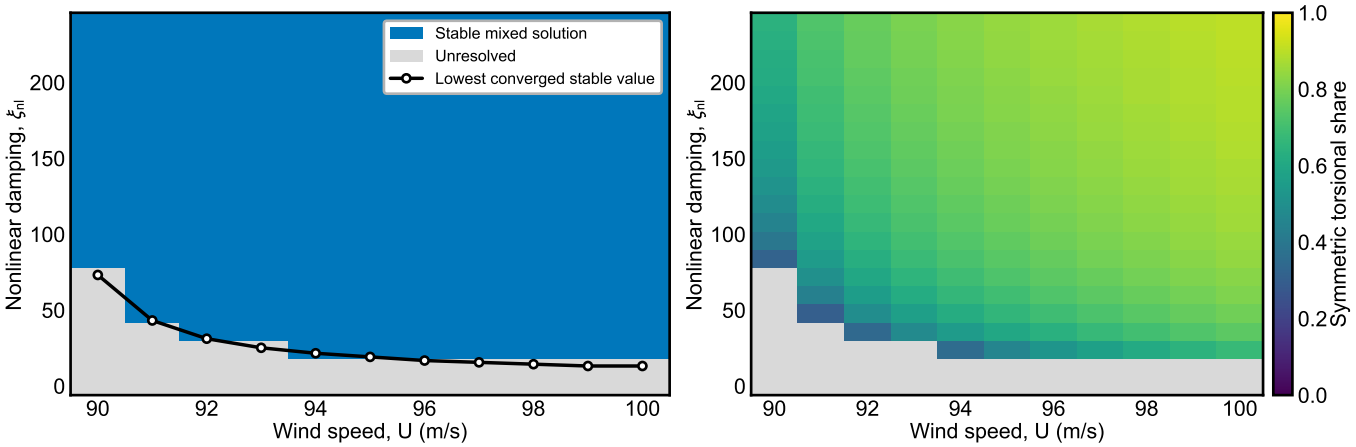

(a) Mixed-branch classification

(b) Symmetric torsional share

Fig. 13: Mixed-response continuation for different wind speeds and assumed damping coefficients.

Table 2: Lowest computed damping values for locally stable mixed responses.

U (m/s)	$U/U_{F,2}$	$\xi_{\mathrm{nl}}^{\mathrm{unr}}$	$\xi_{\mathrm{nl}}^{\mathrm{found}}$
90	1.015	72.0	73.2
94	1.060	20.4	21.6
100	1.127	12.0	13.2

Table 3 compares the responses for different assumed damping coefficients at $U = 94$ m/s. As the damping increases, the antisymmetric amplitude decreases, the symmetric share of the torsional amplitude increases, and the small amplitude and relative-phase perturbations decay faster. The antisymmetric reduction is measured relative to the pure response at $\xi_{\mathrm{nl}} = 0$; more-negative values of $\max \mathrm{Re}\, \lambda_{\perp}$ indicate faster perturbation decay.

The calculated responses show that selective amplitude-dependent dissipation reduces the antisymmetric amplitude and produces locally orbitally stable mixed responses on the

Table 3: Damping sensitivity at $U = 94$ m/s.

ξ_{nl}	Symmetric torsional share	Antisymmetric reduction (%)	max Re $\lambda_{\perp}$
24	0.349	68.40	−0.000796
120	0.756	88.33	−0.005785
240	0.822	91.90	−0.006548

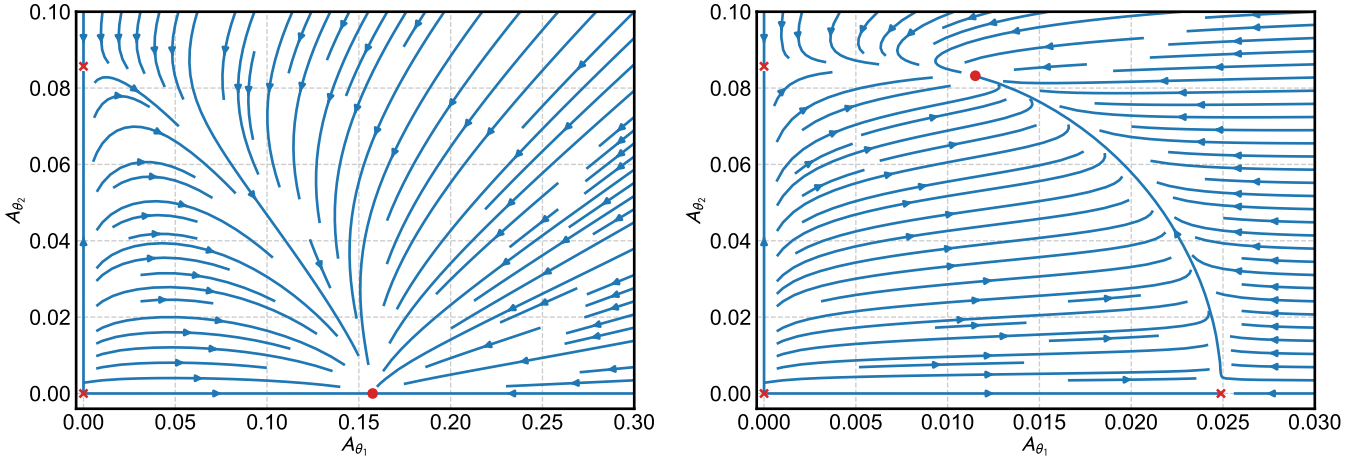

(a) $\xi_{\mathrm{nl}} = 0$.

(b) $\xi_{\mathrm{nl}} = 120$.

Fig. 14: Torsional-amplitude vector fields at fixed phase and $U = 94$ m/s with the assumed damping (a) off and (b) on. Filled circles mark responses that attract nearby amplitude states in this projection; crosses mark non-attracting responses.

computed branches. The stability result applies to the averaged amplitude-and-phase system. Finite-time perturbation comparisons with the original equations at $\xi_{\mathrm{nl}} = 120$ support the predicted decay over the tested histories. The uncalibrated damping term is a candidate mechanism for the observed direction of response change. Measurements of amplitude-dependent energy loss are needed to test the predicted relation between antisymmetric amplitude and dissipation and to assess this mechanism together with other structural and aerodynamic effects.

The quantitative predictions depend on the specified Maanshan inputs and reduced-order assumptions. The damping sweep is a deterministic sensitivity analysis and does not propagate uncertainty in the experiments, aerodynamic fits, or FEM inputs.

The reduction applies to two response patterns that are uncoupled at small amplitude under the stated bridge-symmetry, symmetric aerodynamic weighting, and modal-damping assumptions. As the amplitudes increase, the interaction remains weak, and each response is concentrated near a dominant frequency with slowly varying amplitude and phase. The aerodynamic scope of the reduced formulation is limited by these narrowband conditions. When the bridge or aerodynamic configuration is asymmetric, branch tracking requires the full four-mode linear aerodynamic matrix, with one trial reduced frequency applied throughout the matrix.

6 Conclusions

In this study, a four-mode averaged formulation is established to estimate the nonlinear coupled flutter response while retaining the separate frequencies of the symmetric and antisymmetric vertical–torsional patterns. The formulation includes their symmetry-dependent nonlinear interaction and gives the amplitude and relative-phase evolution from flutter onset to sustained response. The separate-pair and four-mode calculations give the same onset speeds, 71.9 and 88.7 m/s. The baseline time histories and fixed-phase amplitude projection show sustained antisymmetric dominance above the symmetric onset, indicating the effect of nonlinear interaction on response selection.

The amplitude-dependent damping term $-\xi_{\mathrm{nl}}\theta_1^2\dot{\theta}_1$ is introduced to investigate selective dissipation from antisymmetric torsional motion. At $U = 94$ m/s and the assumed coefficient $\xi_{\mathrm{nl}} = 120$, the antisymmetric normalized torsional amplitude decreases by 88.33% relative to the undamped pure response, and the symmetric share of the total normalized torsional amplitude reaches 75.6%. The mixed response is locally orbitally stable in the averaged amplitude-and-phase system. At $\xi_{\mathrm{nl}} = 120$, locally stable mixed responses are obtained across the tested 90–100 m/s grid. Increasing the assumed damping favors the symmetric response and extends the computed stable mixed-response branches to lower wind speeds.

For the tested 600-cycle histories at 90, 94, and 100 m/s, the averaged and original equations agree closely in the late-time response. The imposed small perturbations decay in the original equations, supporting the predicted local recovery over these histories. The transient discrepancy increases toward the upper end of the tested wind-speed range.

The formulation provides a method for estimating sustained coupled flutter amplitudes and their local recovery from small perturbations while retaining both response frequencies. The proposed dissipation mechanism predicts an increase in energy loss with antisymmetric amplitude, which can be examined by free-decay tests and work per vibration cycle.

References

[1] Wang, H., Zou, K., Li, A., Jiao, C.: Parameter effects on the dynamic characteristics of a super-long-span triple-tower suspension bridge. Journal of Zhejiang university-science A **11**(5), 305–316 (2010)

[2] Larsen, A.: Aerodynamics of the tacoma narrows bridge-60 years later. Structural Engineering International **10**(4), 243–248 (2000)

[3] Wang, H., Tao, T., Zhou, R., Hua, X., Kareem, A.: Parameter sensitivity study on flutter stability of a long-span triple-tower suspension bridge. Journal of Wind Engineering and Industrial Aerodynamics **128**, 12–21 (2014)

[4] Scanlan, R.: The action of flexible bridges under wind, i: flutter theory. Journal of Sound and Vibration **60**(2), 187–199 (1978)

[5] Theodorsen, T.: General theory of aerodynamic instability and the mechanism of flutter. Technical Report 496, National Advisory Committee for Aeronautics (1935)

[6] Zhu, L.-D., Gao, G.-Z., Zhu, Q.: Recent advances, future application and challenges in nonlinear flutter theory of long span bridges. Journal of Wind Engineering and Industrial Aerodynamics **206**, 104307 (2020)

[7] Ying, X., Xu, F., Zhang, M., Zhang, Z.: Numerical explorations of the limit cycle flutter characteristics of a bridge deck. Journal of Wind Engineering and Industrial Aerodynamics **169**, 30–38 (2017)

[8] Gao, G., Zhu, L., Han, W., Li, J.: Nonlinear post-flutter behavior and self-excited force model of a twin-side-girder bridge deck. Journal of Wind Engineering and Industrial Aerodynamics **177**, 227–241 (2018)

[9] Diana, G., Rocchi, D., Argentini, T., Muggiasca, S.: Aerodynamic instability of a bridge deck section model: Linear and nonlinear approach to force modeling. Journal of Wind Engineering and Industrial Aerodynamics **98**(6-7), 363–374 (2010)

[10] Borri, C., Costa, C.: Quasi-steady analysis of a two-dimensional bridge deck element. Computers & structures **82**(13-14), 993–1006 (2004)

[11] Wu, T., Kareem, A., Ge, Y.: Linear and nonlinear aeroelastic analysis frameworks for cable-supported bridges. Nonlinear Dynamics **74**(3), 487–516 (2013)

[12] Gao, G., Zhu, L., Li, J., Han, W., Yao, B.: A novel two-degree-of-freedom model of nonlinear self-excited force for coupled flutter instability of bridge decks. Journal of Sound and Vibration **480**, 115406 (2020)

[13] Zhao, L., Xie, X., Zhan, Y.-y., Cui, W., Ge, Y.-j., Xia, Z.-c., Xu, S.-q., Zeng, M.: A novel forced motion apparatus with potential applications in structural engineering. Journal of Zhejiang University-SCIENCE A **21**(7), 593–608 (2020)

[14] Katsuchi, H., Jones, N., Scanlan, R., Akiyama, H.: Multi-mode flutter and buffeting analysis of the akashi-kaikyo bridge. Journal of Wind Engineering and Industrial Aerodynamics **77–78**, 431–441 (1998) https://doi.org/10.1016/S0167-6105(98)00162-7

[15] Hua, X., Chen, Z.: Full-order and multimode flutter analysis using ansys. Finite

Elements in Analysis and Design **44**(9-10), 537–551 (2008)

[16] Ge, Y., Tanaka, H.: Aerodynamic flutter analysis of cable-supported bridges by multi-mode and full-mode approaches. Journal of Wind Engineering and Industrial Aerodynamics **86**(2-3), 123–153 (2000)

[17] Wu, B., Liao, H., Shen, H., Wang, Q., Mei, H., Li, Z.: Multimode coupled nonlinear flutter analysis for long-span bridges by considering dependence of flutter derivatives on vibration amplitude. Computers & Structures **260**, 106700 (2022)

[18] Li, K., Han, Y., Cai, C., Zhang, W., Song, J., Yan, H.: A nonlinear numerical scheme to investigate the influence of geometric nonlinearity on post-flutter responses of bridges. Nonlinear Dynamics **112**(9), 6813–6845 (2024) https://doi.org/10.1007/s11071-024-09298-0

[19] Zhang, W.-m., Ge, Y.-j.: Wind tunnel investigation on flutter and buffeting of a three-tower suspension bridge. Wind & structures **24**(4), 367–384 (2017)

[20] Zhang, W.: Study on wind-resistance property of multi-main-span suspension bridges and full process of wind induced hazard evolution (in chinese). PhD thesis, Tongji University (2011)

[21] Zhang, W.-m., Qian, K.-r., Ge, Y.-j.: Research on flutter-mode transition of a triple-tower suspension bridge based on structural nonlinearity. Structures **34**, 787–803 (2021)

[22] Zhang, W.-m., Feng, D.-d., Zhao, L.-m., Ge, Y.-j.: A deep learning-based method for full-bridge flutter analysis considering aerodynamic and geometric nonlinearities. Computers & Structures **310**, 107693 (2025)

[23] Zhang, Q., Tang, H.-q., Yang, G.-w.: Selection of a structural system for a three-tower suspension bridge of Maanshan Yangtze River Highway Bridge.

Structural Engineering International **22**(1), 139–143 (2012) https://doi.org/10.2749/101686612X13216060213590

[24] Ko, J., Xue, S., Xu, Y.: Modal analysis of suspension bridge deck units in erection stage. Engineering structures **20**(12), 1102–1112 (1998)

[25] Ma, T., Cui, W., Gao, T., Liu, S., Zhao, L., Ge, Y.: Data-based autonomously discovering method for nonlinear aerodynamic force of quasi-flat plate. Physics of Fluids **35**(2), 024103 (2023) https://doi.org/10.1063/5.0133526

Statements and Declarations

Funding

The authors gratefully acknowledge the support of the Department of Science and Technology of Guangxi Zhuang Autonomous Region (2026GKLT0253020) and the National Natural Science Foundation of China (52478552 and 52378527). Any opinions, findings and conclusions are those of the authors and do not necessarily reflect the views of the above agencies.

Competing Interests

The authors have no relevant financial or non-financial interests to disclose.

Author Contributions

The conception and design of the study was a collaborative effort between all authors. Wei Cui was responsible for the conception, modeling and computation. Wei Cui wrote the first draft of the manuscript, and Lin Zhao supervised the entire study. Both Wei Cui and Lin Zhao provided financial support for the research. All authors read and approved the final version of the manuscript.

Data Availability

The datasets generated and analyzed during the current study are not publicly available due to security concerns of the owner of the bridge but are available from the corresponding author on reasonable request.

Use of Generative AI

OpenAI Codex with GPT-6 Astra was used during manuscript preparation to assist with LaTeX formatting and language editing. The authors remain responsible for verifying and approving the submitted version of manuscript.

A Detailed derivation of the coupled flutter equations

A.1 Governing equations before modal symmetry reduction

By substituting the two vertical and two torsional modal contributions into the aerodynamic force model, the complete four-mode governing equations are obtained as follows. All aerodynamic interaction terms are retained before applying the modal symmetry conditions.

$$\begin{aligned}\ddot{y}_1 + 2\xi_{y_1} K_{y_1}\dot{y}_1 + K_{y_1}^2 y_1 = \frac{m^*_{y_1}}{\phi_{y_1 y_1}}[&\phi_{y_1 y_1} K_1 H_1^*(K_1)\dot{y}_1 + \phi_{y_1 y_2} K_2 H_1^*(K_2)\dot{y}_2 + \phi_{y_1\theta_1} K_1 H_2^*(K_1)\dot{\theta}_1 + \phi_{y_1\theta_2} K_2 H_2^*(K_2)\dot{\theta}_2 + \\ &\phi_{y_1\theta_1} K_1^2 H_3^*(K_1)\theta_1 + \phi_{y_1\theta_2} K_2^2 H_3^*(K_2)\theta_2 + \phi_{y_1 y_1} K_1^2 H_4^*(K_1) y_1 + \phi_{y_1 y_2} K_2^2 H_4^*(K_2) y_2 + \\ &\phi_{\theta_1^2 y_1} b_1^{(1)} K_1^2\theta_1\dot{\theta}_1 + \phi_{\theta_1\theta_2 y_1} b_1^{(1)} K_1^2\theta_1\dot{\theta}_2 + \phi_{\theta_1\theta_2 y_1} b_1^{(1)} K_1 K_2\theta_2\dot{\theta}_1 + \phi_{\theta_2^2 y_1} b_1^{(1)} K_1 K_2\theta_2\dot{\theta}_2 + \\ &\phi_{\theta_1^3 y_1} b_2^{(1)} K_1^2\theta_1\dot{\theta}_1^2 + \phi_{\theta_1^2\theta_2 y_1} b_2^{(1)} K_1 K_2\theta_2\dot{\theta}_1^2 + 2\phi_{\theta_1^2\theta_2 y_1} b_2^{(1)} K_1^2\theta_1\dot{\theta}_1\dot{\theta}_2 + \\ &2\phi_{\theta_1\theta_2^2 y_1} b_2^{(1)} K_1 K_2\theta_2\dot{\theta}_1\dot{\theta}_2 + \phi_{\theta_1\theta_2^2 y_1} b_2^{(1)} K_1^2\theta_1\dot{\theta}_2^2 + \phi_{\theta_2^3 y_1} b_2^{(1)} K_1 K_2\theta_2\dot{\theta}_2^2]\end{aligned} \tag{A.1a}$$

$$\begin{aligned}\ddot{y}_2 + 2\xi_{y_2} K_{y_2}\dot{y}_2 + K_{y_2}^2 y_2 = \frac{m^*_{y_2}}{\phi_{y_2 y_2}}[&\phi_{y_1 y_2} K_1 H_1^*(K_1)\dot{y}_1 + \phi_{y_2 y_2} K_2 H_1^*(K_2)\dot{y}_2 + \phi_{y_2\theta_1} K_1 H_2^*(K_1)\dot{\theta}_1 + \phi_{y_2\theta_2} K_2 H_2^*(K_2)\dot{\theta}_2 + \\ &\phi_{y_2\theta_1} K_1^2 H_3^*(K_1)\theta_1 + \phi_{y_2\theta_2} K_2^2 H_3^*(K_2)\theta_2 + \phi_{y_1 y_2} K_1^2 H_4^*(K_1) y_1 + \phi_{y_2 y_2} K_2^2 H_4^*(K_2) y_2 + \\ &\phi_{\theta_1^2 y_2} b_1^{(2)} K_1 K_2\theta_1\dot{\theta}_1 + \phi_{\theta_1\theta_2 y_2} b_1^{(2)} K_1 K_2\theta_1\dot{\theta}_2 + \phi_{\theta_1\theta_2 y_2} b_1^{(2)} K_2^2\theta_2\dot{\theta}_1 + \phi_{\theta_2^2 y_2} b_1^{(2)} K_2^2\theta_2\dot{\theta}_2 + \\ &\phi_{\theta_1^3 y_2} b_2^{(2)} K_1 K_2\theta_1\dot{\theta}_1^2 + \phi_{\theta_1^2\theta_2 y_2} b_2^{(2)} K_2^2\theta_2\dot{\theta}_1^2 + 2\phi_{\theta_1^2\theta_2 y_2} b_2^{(2)} K_1 K_2\theta_1\dot{\theta}_1\dot{\theta}_2 + \\ &2\phi_{\theta_1\theta_2^2 y_2} b_2^{(2)} K_2^2\theta_2\dot{\theta}_1\dot{\theta}_2 + \phi_{\theta_1\theta_2^2 y_2} b_2^{(2)} K_1 K_2\theta_1\dot{\theta}_2^2 + \phi_{\theta_2^3 y_2} b_2^{(2)} K_2^2\theta_2\dot{\theta}_2^2]\end{aligned} \tag{A.1b}$$

$$\begin{aligned}\ddot{\theta}_1 + 2\xi_{\theta_1} K_{\theta_1}\dot{\theta}_1 + K_{\theta_1}^2\theta_1 = \frac{m^*_{\theta_1}}{\phi_{\theta_1\theta_1}}[&\phi_{y_1\theta_1} K_1 A_1^*(K_1)\dot{y}_1 + \phi_{y_2\theta_1} K_2 A_1^*(K_2)\dot{y}_2 + \phi_{\theta_1\theta_1} K_1 A_2^*(K_1)\dot{\theta}_1 + \phi_{\theta_1\theta_2} K_2 A_2^*(K_2)\dot{\theta}_2 + \\ &\phi_{\theta_1\theta_1} K_1^2 A_3^*(K_1)\theta_1 + \phi_{\theta_1\theta_2} K_2^2 A_3^*(K_2)\theta_2 + \phi_{y_1\theta_1} K_1^2 A_4^*(K_1) y_1 + \phi_{y_2\theta_1} K_2^2 A_4^*(K_2) y_2 + \\ &\phi_{\theta_1^3} c_1^{(1)} K_1\dot{\theta}_1^2 + 2\phi_{\theta_1^2\theta_2} c_1^{(1)} K_1\dot{\theta}_1\dot{\theta}_2 + \phi_{\theta_1\theta_2^2} c_1^{(1)} K_1\dot{\theta}_2^2 + \\ &\phi_{\theta_1^3} c_2^{(1)} K_1^3\theta_1^2 + 2\phi_{\theta_1^2\theta_2} c_2^{(1)} K_1^2 K_2\theta_1\theta_2 + \phi_{\theta_1\theta_2^2} c_2^{(1)} K_1 K_2^2\theta_2^2 + \\ &\phi_{\theta_1^4} c_3^{(1)} K_1\dot{\theta}_1^3 + 3\phi_{\theta_1^3\theta_2} c_3^{(1)} K_1\dot{\theta}_1^2\dot{\theta}_2 + 3\phi_{\theta_1^2\theta_2^2} c_3^{(1)} K_1\dot{\theta}_1\dot{\theta}_2^2 + \phi_{\theta_1\theta_2^3} c_3^{(1)} K_1\dot{\theta}_2^3]\end{aligned} \tag{A.1c}$$

$$\begin{aligned}\ddot{\theta}_2 + 2\xi_{\theta_2} K_{\theta_2}\dot{\theta}_2 + K_{\theta_2}^2\theta_2 = \frac{m^*_{\theta_2}}{\phi_{\theta_2\theta_2}}[&\phi_{y_1\theta_2} K_1 A_1^*(K_1)\dot{y}_1 + \phi_{y_2\theta_2} K_2 A_1^*(K_2)\dot{y}_2 + \phi_{\theta_1\theta_2} K_1 A_2^*(K_1)\dot{\theta}_1 + \phi_{\theta_2\theta_2} K_2 A_2^*(K_2)\dot{\theta}_2 + \\ &\phi_{\theta_1\theta_2} K_1^2 A_3^*(K_1)\theta_1 + \phi_{\theta_2\theta_2} K_2^2 A_3^*(K_2)\theta_2 + \phi_{y_1\theta_2} K_1^2 A_4^*(K_1) y_1 + \phi_{y_2\theta_2} K_2^2 A_4^*(K_2) y_2 + \\ &\phi_{\theta_1^2\theta_2} c_1^{(2)} K_2\dot{\theta}_1^2 + 2\phi_{\theta_1\theta_2^2} c_1^{(2)} K_2\dot{\theta}_1\dot{\theta}_2 + \phi_{\theta_2^3} c_1^{(2)} K_2\dot{\theta}_2^2 + \\ &\phi_{\theta_1^2\theta_2} c_2^{(2)} K_1^2 K_2\theta_1^2 + 2\phi_{\theta_1\theta_2^2} c_2^{(2)} K_1 K_2^2\theta_1\theta_2 + \phi_{\theta_2^3} c_2^{(2)} K_2^3\theta_2^2 + \\ &\phi_{\theta_1^3\theta_2} c_3^{(2)} K_2\dot{\theta}_1^3 + 3\phi_{\theta_1^2\theta_2^2} c_3^{(2)} K_2\dot{\theta}_1^2\dot{\theta}_2 + 3\phi_{\theta_1\theta_2^3} c_3^{(2)} K_2\dot{\theta}_1\dot{\theta}_2^2 + \phi_{\theta_2^4} c_3^{(2)} K_2\dot{\theta}_2^3]\end{aligned} \tag{A.1d}$$

where (y_1, θ_1) and (y_2, θ_2) are the antisymmetric (odd) and symmetric (even) vertical–torsional modal coordinates about midspan, respectively. The modal-product factors are calculated by Eq. (15) to account for the spanwise distribution of aerodynamic loading.

A.2 Derivation of the amplitude and phase evolution equations

The complexification-averaging method is used to derive the amplitude and phase evolution equations of the four-mode flutter response. By separating the slow complex envelopes from the fast oscillatory components, the nonlinear response evolution and interaction between the two flutter modes can be evaluated.

The derivation is based on the formal near-1 : 1 scaling $K_2 - K_1 = \mathcal{O}(\epsilon)$, where ϵ is the formal small parameter for the frequency separation near internal resonance. The time-independent and frequency-difference terms are retained, while the rapidly oscillating fundamental- and sum-frequency terms are averaged out. For the numerical cases in this study, the relative detuning is finite. The corresponding accuracy is assessed by comparing matched integrations of the original and averaged equations in Figure 12. The autonomous continuation uses the time-independent subsystem defined in Section 3.3.

By expanding the nonlinear aerodynamic terms, the equation of the antisymmetric vertical response is expressed as

$$
\begin{aligned}
\dot{\psi}_{y_1} - \imath K_1 \frac{\psi_{y_1} + \psi^*_{y_1}}{2} + 2\xi_{y_1} K_{y_1} \frac{\psi_{y_1} + \psi^*_{y_1}}{2} + K_{y_1}^2 \frac{\psi_{y_1} - \psi^*_{y_1}}{2\imath K_1} = \frac{m^*_{y_1}}{\phi_{y_1 y_1}} \Bigg[& \phi_{y_1 y_1} K_1 H_1^*(K_1) \frac{\psi_{y_1} + \psi^*_{y_1}}{2} + \phi_{y_1 \theta_1} K_1 H_2^*(K_1) \frac{\psi_{\theta_1} + \psi^*_{\theta_1}}{2} \\
& + \phi_{y_1 \theta_1} K_1^2 H_3^*(K_1) \frac{\psi_{\theta_1} - \psi^*_{\theta_1}}{2\imath K_1} + \phi_{y_1 y_1} K_1^2 H_4^*(K_1) \frac{\psi_{y_1} - \psi^*_{y_1}}{2\imath K_1} + \phi_{\theta_1 \theta_2 y_1} b_1^{(1)} \frac{K_1^2}{4\imath K_1} \left(\psi_{\theta_1} \psi_{\theta_2} + \psi_{\theta_1} \psi^*_{\theta_2} - \psi^*_{\theta_1} \psi_{\theta_2} - \psi^*_{\theta_1} \psi^*_{\theta_2} \right) \\
& + \phi_{\theta_1 \theta_2 y_1} b_1^{(1)} \frac{K_1 K_2}{4\imath K_2} \left(\psi_{\theta_1} \psi_{\theta_2} + \psi^*_{\theta_1} \psi_{\theta_2} - \psi_{\theta_1} \psi^*_{\theta_2} - \psi^*_{\theta_1} \psi^*_{\theta_2} \right) + \phi_{\theta_1^3 y_1} b_2^{(1)} \frac{K_1^2}{8\imath K_1} \left(\psi^3_{\theta_1} + \psi^2_{\theta_1} \psi^*_{\theta_1} - \psi_{\theta_1} \psi^{*2}_{\theta_1} - \psi^{*3}_{\theta_1} \right) \\
& + 2\phi_{\theta_1 \theta_2^2 y_1} b_2^{(1)} \frac{K_1 K_2}{8\imath K_2} \left(\psi_{\theta_1} \psi^2_{\theta_2} + \psi^*_{\theta_1} \psi^2_{\theta_2} - \psi_{\theta_1} \psi^{*2}_{\theta_2} - \psi^*_{\theta_1} \psi^{*2}_{\theta_2} \right) + \phi_{\theta_1 \theta_2^2 y_1} b_2^{(1)} \frac{K_1^2}{8\imath K_1} \Big(\psi_{\theta_1} \psi^2_{\theta_2} + 2\psi_{\theta_1} \psi_{\theta_2} \psi^*_{\theta_2} + \psi_{\theta_1} \psi^{*2}_{\theta_2} \\
& - \psi^*_{\theta_1} \psi^2_{\theta_2} - 2\psi^*_{\theta_1} \psi_{\theta_2} \psi^*_{\theta_2} - \psi^*_{\theta_1} \psi^{*2}_{\theta_2} \Big) \Bigg]
\end{aligned}
\tag{A.2}
$$

Then, each complex response and its conjugate are decomposed into slow and fast components:

$$
\begin{aligned}
\psi_{y_j} &= \phi_{y_j} e^{\imath K_j \tau}, \qquad & \psi^*_{y_j} &= \phi^*_{y_j} e^{-\imath K_j \tau}, \\
\psi_{\theta_j} &= \phi_{\theta_j} e^{\imath K_j \tau}, \qquad & \psi^*_{\theta_j} &= \phi^*_{\theta_j} e^{-\imath K_j \tau}, \qquad j = 1, 2.
\end{aligned}
$$

where ϕ_{y_j} and ϕ_{θ_j} are the slow complex envelopes of the vertical and torsional responses, respectively. For constant K_1, the derivative in Eq. (A.2) becomes $\dot{\psi}_{y_1} = \left(\dot{\phi}_{y_1} + \imath K_1 \phi_{y_1} \right) e^{\imath K_1 \tau}$. Substitution into Eq. (A.2) gives

$$
\begin{aligned}
&\left(\dot{\phi}_{y_1}+\iota K_1\phi_{y_1}\right)e^{\iota K_1\tau}-\frac{\iota K_1}{2}\left(\phi_{y_1}e^{\iota K_1\tau}+\phi_{y_1}^{*}e^{-\iota K_1\tau}\right)+\xi_{y_1}K_{y_1}\left(\phi_{y_1}e^{\iota K_1\tau}+\phi_{y_1}^{*}e^{-\iota K_1\tau}\right)-\frac{\iota K_{y_1}^{2}}{2K_1}\left(\phi_{y_1}e^{\iota K_1\tau}-\phi_{y_1}^{*}e^{-\iota K_1\tau}\right)\\
&=\frac{m_{y_1}^{*}}{\phi_{y_1y_1}}\Bigg[\frac{\phi_{y_1y_1}K_1H_1^{*}(K_1)}{2}\left(\phi_{y_1}e^{\iota K_1\tau}+\phi_{y_1}^{*}e^{-\iota K_1\tau}\right)+\frac{\phi_{y_1\theta_1}K_1H_2^{*}(K_1)}{2}\left(\phi_{\theta_1}e^{\iota K_1\tau}+\phi_{\theta_1}^{*}e^{-\iota K_1\tau}\right)-\frac{\iota\phi_{y_1\theta_1}K_1H_3^{*}(K_1)}{2}\left(\phi_{\theta_1}e^{\iota K_1\tau}-\phi_{\theta_1}^{*}e^{-\iota K_1\tau}\right)\\
&-\frac{\iota\phi_{y_1y_1}K_1H_4^{*}(K_1)}{2}\left(\phi_{y_1}e^{\iota K_1\tau}-\phi_{y_1}^{*}e^{-\iota K_1\tau}\right)-\frac{\iota K_1}{2}\phi_{\theta_1\theta_2y_1}b_1^{(1)}\Big(\phi_{\theta_1}\phi_{\theta_2}e^{\iota(K_1+K_2)\tau}-\phi_{\theta_1}^{*}\phi_{\theta_2}^{*}e^{-\iota(K_1+K_2)\tau}\Big)\\
&-\frac{\iota K_1}{8}\phi_{\theta_1^3y_1}b_2^{(1)}\Big(\phi_{\theta_1}^{3}e^{3\iota K_1\tau}+\phi_{\theta_1}^{2}\phi_{\theta_1}^{*}e^{\iota K_1\tau}-\phi_{\theta_1}\phi_{\theta_1}^{*2}e^{-\iota K_1\tau}-\phi_{\theta_1}^{*3}e^{-3\iota K_1\tau}\Big)\\
&-\frac{\iota K_1}{4}\phi_{\theta_1\theta_2^2y_1}b_2^{(1)}\Big(\phi_{\theta_1}\phi_{\theta_2}^{2}e^{\iota(K_1+2K_2)\tau}+\phi_{\theta_1}^{*}\phi_{\theta_2}^{2}e^{\iota(2K_2-K_1)\tau}-\phi_{\theta_1}\phi_{\theta_2}^{*2}e^{\iota(K_1-2K_2)\tau}-\phi_{\theta_1}^{*}\phi_{\theta_2}^{*2}e^{-\iota(K_1+2K_2)\tau}\Big)\\
&-\frac{\iota K_1}{8}\phi_{\theta_1\theta_2^2y_1}b_2^{(1)}\Big(\phi_{\theta_1}\phi_{\theta_2}^{2}e^{\iota(K_1+2K_2)\tau}+2\phi_{\theta_1}\phi_{\theta_2}\phi_{\theta_2}^{*}e^{\iota K_1\tau}+\phi_{\theta_1}\phi_{\theta_2}^{*2}e^{\iota(K_1-2K_2)\tau}-\phi_{\theta_1}^{*}\phi_{\theta_2}^{2}e^{\iota(2K_2-K_1)\tau}-2\phi_{\theta_1}^{*}\phi_{\theta_2}\phi_{\theta_2}^{*}e^{-\iota K_1\tau}-\phi_{\theta_1}^{*}\phi_{\theta_2}^{*2}e^{-\iota(K_1+2K_2)\tau}\Big)\Bigg]
\end{aligned}
\tag{A.3}
$$

Dividing Eq. (A.3) by $e^{\iota K_1\tau}$ gives the evolution equation of the complex envelope:

$$
\begin{aligned}
&\dot{\phi}_{y_1}+\iota K_1\phi_{y_1}-\frac{\iota K_1}{2}\left(\phi_{y_1}+\phi_{y_1}^{*}e^{-2\iota K_1\tau}\right)+\xi_{y_1}K_{y_1}\left(\phi_{y_1}+\phi_{y_1}^{*}e^{-2\iota K_1\tau}\right)-\frac{\iota K_{y_1}^{2}}{2K_1}\left(\phi_{y_1}-\phi_{y_1}^{*}e^{-2\iota K_1\tau}\right)\\
&=\frac{m_{y_1}^{*}}{\phi_{y_1y_1}}\Bigg[\frac{\phi_{y_1y_1}K_1H_1^{*}(K_1)}{2}\left(\phi_{y_1}+\phi_{y_1}^{*}e^{-2\iota K_1\tau}\right)+\frac{\phi_{y_1\theta_1}K_1H_2^{*}(K_1)}{2}\left(\phi_{\theta_1}+\phi_{\theta_1}^{*}e^{-2\iota K_1\tau}\right)-\frac{\iota\phi_{y_1\theta_1}K_1H_3^{*}(K_1)}{2}\left(\phi_{\theta_1}-\phi_{\theta_1}^{*}e^{-2\iota K_1\tau}\right)\\
&-\frac{\iota\phi_{y_1y_1}K_1H_4^{*}(K_1)}{2}\left(\phi_{y_1}-\phi_{y_1}^{*}e^{-2\iota K_1\tau}\right)-\frac{\iota K_1}{2}\phi_{\theta_1\theta_2y_1}b_1^{(1)}\Big(\phi_{\theta_1}\phi_{\theta_2}e^{\iota K_2\tau}-\phi_{\theta_1}^{*}\phi_{\theta_2}^{*}e^{-\iota(2K_1+K_2)\tau}\Big)\\
&-\frac{\iota K_1}{8}\phi_{\theta_1^3y_1}b_2^{(1)}\Big(\phi_{\theta_1}^{3}e^{2\iota K_1\tau}+\phi_{\theta_1}^{2}\phi_{\theta_1}^{*}-\phi_{\theta_1}\phi_{\theta_1}^{*2}e^{-2\iota K_1\tau}-\phi_{\theta_1}^{*3}e^{-4\iota K_1\tau}\Big)\\
&-\frac{\iota K_1}{4}\phi_{\theta_1\theta_2^2y_1}b_2^{(1)}\Big(\phi_{\theta_1}\phi_{\theta_2}^{2}e^{2\iota K_2\tau}+\phi_{\theta_1}^{*}\phi_{\theta_2}^{2}e^{2\iota(K_2-K_1)\tau}-\phi_{\theta_1}\phi_{\theta_2}^{*2}e^{-2\iota K_2\tau}-\phi_{\theta_1}^{*}\phi_{\theta_2}^{*2}e^{-2\iota(K_1+K_2)\tau}\Big)\\
&-\frac{\iota K_1}{8}\phi_{\theta_1\theta_2^2y_1}b_2^{(1)}\Big(\phi_{\theta_1}\phi_{\theta_2}^{2}e^{2\iota K_2\tau}+2\phi_{\theta_1}\phi_{\theta_2}\phi_{\theta_2}^{*}+\phi_{\theta_1}\phi_{\theta_2}^{*2}e^{-2\iota K_2\tau}-\phi_{\theta_1}^{*}\phi_{\theta_2}^{2}e^{2\iota(K_2-K_1)\tau}-2\phi_{\theta_1}^{*}\phi_{\theta_2}\phi_{\theta_2}^{*}e^{-2\iota K_1\tau}-\phi_{\theta_1}^{*}\phi_{\theta_2}^{*2}e^{-2\iota(K_1+K_2)\tau}\Big)\Bigg]
\end{aligned}
\tag{A.4}
$$

Under the near-1 : 1 assumption $K_2-K_1=\mathcal{O}(\epsilon)$, first-order averaging retains the time-independent terms and the slow modulation $e^{2\iota(K_2-K_1)\tau}$ caused by the frequency difference. By averaging out the fundamental- and sum-frequency terms in Eq. (A.4), the antisymmetric vertical response is obtained as

$$
\begin{aligned}
\dot{\phi}_{y_1}+\xi_{y_1}K_{y_1}\phi_{y_1}-\frac{\iota\left(K_{y_1}^{2}-K_1^{2}\right)}{2K_1}\phi_{y_1}=\frac{m_{y_1}^{*}}{\phi_{y_1y_1}}\Bigg[&\frac{\phi_{y_1y_1}K_1}{2}\left(H_1^{*}(K_1)-\iota H_4^{*}(K_1)\right)\phi_{y_1}+\frac{\phi_{y_1\theta_1}K_1}{2}\left(H_2^{*}(K_1)-\iota H_3^{*}(K_1)\right)\phi_{\theta_1}\\
&-\frac{\iota K_1}{8}\phi_{\theta_1^3y_1}b_2^{(1)}\phi_{\theta_1}^{2}\phi_{\theta_1}^{*}-\frac{\iota K_1}{8}\phi_{\theta_1\theta_2^2y_1}b_2^{(1)}\Big(2\phi_{\theta_1}\phi_{\theta_2}\phi_{\theta_2}^{*}+\phi_{\theta_1}^{*}\phi_{\theta_2}^{2}e^{2\iota(K_2-K_1)\tau}\Big)\Bigg].
\end{aligned}
\tag{A.5}
$$

Similarly, the equation of the symmetric vertical response is expanded as

$$
\begin{aligned}
\dot{\psi}_{y_2}-\iota K_2\frac{\psi_{y_2}+\psi_{y_2}^{*}}{2}+2\xi_{y_2}K_{y_2}\frac{\psi_{y_2}+\psi_{y_2}^{*}}{2}+K_{y_2}^{2}\frac{\psi_{y_2}-\psi_{y_2}^{*}}{2\iota K_2}=\frac{m_{y_2}^{*}}{\phi_{y_2y_2}}\Bigg[&\phi_{y_2y_2}K_2H_1^{*}(K_2)\frac{\psi_{y_2}+\psi_{y_2}^{*}}{2}+\phi_{y_2\theta_2}K_2H_2^{*}(K_2)\frac{\psi_{\theta_2}+\psi_{\theta_2}^{*}}{2}\\
&+\phi_{y_2\theta_2}K_2^{2}H_3^{*}(K_2)\frac{\psi_{\theta_2}-\psi_{\theta_2}^{*}}{2\iota K_2}+\phi_{y_2y_2}K_2^{2}H_4^{*}(K_2)\frac{\psi_{y_2}-\psi_{y_2}^{*}}{2\iota K_2}+\phi_{\theta_1^2y_2}b_1^{(2)}\frac{K_1K_2}{4\iota K_1}\left(\psi_{\theta_1}^{2}-\psi_{\theta_1}^{*2}\right)+\phi_{\theta_2^2y_2}b_1^{(2)}\frac{K_2^{2}}{4\iota K_2}\left(\psi_{\theta_2}^{2}-\psi_{\theta_2}^{*2}\right)\\
&+\phi_{\theta_1^2\theta_2y_2}b_2^{(2)}\frac{K_2^{2}}{8\iota K_2}\Big(\psi_{\theta_1}^{2}\psi_{\theta_2}+2\psi_{\theta_1}\psi_{\theta_1}^{*}\psi_{\theta_2}+\psi_{\theta_1}^{*2}\psi_{\theta_2}-\psi_{\theta_1}^{2}\psi_{\theta_2}^{*}-2\psi_{\theta_1}\psi_{\theta_1}^{*}\psi_{\theta_2}^{*}-\psi_{\theta_1}^{*2}\psi_{\theta_2}^{*}\Big)\\
&+2\phi_{\theta_1^2\theta_2y_2}b_2^{(2)}\frac{K_1K_2}{8\iota K_1}\Big(\psi_{\theta_1}^{2}\psi_{\theta_2}+\psi_{\theta_1}^{2}\psi_{\theta_2}^{*}-\psi_{\theta_1}^{*2}\psi_{\theta_2}-\psi_{\theta_1}^{*2}\psi_{\theta_2}^{*}\Big)+\phi_{\theta_2^3y_2}b_2^{(2)}\frac{K_2^{2}}{8\iota K_2}\Big(\psi_{\theta_2}^{3}+\psi_{\theta_2}^{2}\psi_{\theta_2}^{*}-\psi_{\theta_2}\psi_{\theta_2}^{*2}-\psi_{\theta_2}^{*3}\Big)\Bigg].
\end{aligned}
\tag{A.6}
$$

For constant K_2, the derivative in Eq. (A.6) becomes $\dot{\psi}_{y_2} = \left(\dot{\phi}_{y_2} + \iota K_2 \phi_{y_2}\right) e^{\iota K_2 \tau}$. Substitution into Eq. (A.6) gives

$$
\begin{aligned}
&\left(\dot{\phi}_{y_2} + \iota K_2 \phi_{y_2}\right) e^{\iota K_2 \tau} - \frac{\iota K_2}{2}\left(\phi_{y_2} e^{\iota K_2 \tau} + \phi_{y_2}^* e^{-\iota K_2 \tau}\right) + \xi_{y_2} K_{y_2}\left(\phi_{y_2} e^{\iota K_2 \tau} + \phi_{y_2}^* e^{-\iota K_2 \tau}\right) - \frac{\iota K_{y_2}^2}{2K_2}\left(\phi_{y_2} e^{\iota K_2 \tau} - \phi_{y_2}^* e^{-\iota K_2 \tau}\right) \\
&= \frac{m_{y_2}^*}{\phi_{y_2 y_2}}\Bigg[\frac{\phi_{y_2 y_2} K_2 H_1^*(K_2)}{2}\left(\phi_{y_2} e^{\iota K_2 \tau} + \phi_{y_2}^* e^{-\iota K_2 \tau}\right) + \frac{\phi_{y_2 \theta_2} K_2 H_2^*(K_2)}{2}\left(\phi_{\theta_2} e^{\iota K_2 \tau} + \phi_{\theta_2}^* e^{-\iota K_2 \tau}\right) - \frac{\iota \phi_{y_2 \theta_2} K_2 H_3^*(K_2)}{2}\left(\phi_{\theta_2} e^{\iota K_2 \tau} - \phi_{\theta_2}^* e^{-\iota K_2 \tau}\right) \\
&\quad - \frac{\iota \phi_{y_2 y_2} K_2 H_4^*(K_2)}{2}\left(\phi_{y_2} e^{\iota K_2 \tau} - \phi_{y_2}^* e^{-\iota K_2 \tau}\right) - \frac{\iota K_2}{4}\phi_{\theta_1^2 y_2} b_1^{(2)}\left(\phi_{\theta_1}^2 e^{2\iota K_1 \tau} - \phi_{\theta_1}^{*2} e^{-2\iota K_1 \tau}\right) - \frac{\iota K_2}{4}\phi_{\theta_2^2 y_2} b_1^{(2)}\left(\phi_{\theta_2}^2 e^{2\iota K_2 \tau} - \phi_{\theta_2}^{*2} e^{-2\iota K_2 \tau}\right) \\
&\quad - \frac{\iota K_2}{8}\phi_{\theta_1^2 \theta_2 y_2} b_2^{(2)}\Big(\phi_{\theta_1}^2 \phi_{\theta_2} e^{\iota(2K_1+K_2)\tau} + 2\phi_{\theta_1}\phi_{\theta_1}^*\phi_{\theta_2} e^{\iota K_2 \tau} + \phi_{\theta_1}^{*2}\phi_{\theta_2} e^{\iota(K_2-2K_1)\tau} - \phi_{\theta_1}^2\phi_{\theta_2}^* e^{\iota(2K_1-K_2)\tau} - 2\phi_{\theta_1}\phi_{\theta_1}^*\phi_{\theta_2}^* e^{-\iota K_2 \tau} - \phi_{\theta_1}^{*2}\phi_{\theta_2}^* e^{-\iota(2K_1+K_2)\tau}\Big) \\
&\quad - \frac{\iota K_2}{4}\phi_{\theta_1^2 \theta_2 y_2} b_2^{(2)}\Big(\phi_{\theta_1}^2 \phi_{\theta_2} e^{\iota(2K_1+K_2)\tau} + \phi_{\theta_1}^2\phi_{\theta_2}^* e^{\iota(2K_1-K_2)\tau} - \phi_{\theta_1}^{*2}\phi_{\theta_2} e^{\iota(K_2-2K_1)\tau} - \phi_{\theta_1}^{*2}\phi_{\theta_2}^* e^{-\iota(2K_1+K_2)\tau}\Big) \\
&\quad - \frac{\iota K_2}{8}\phi_{\theta_2^3 y_2} b_2^{(2)}\Big(\phi_{\theta_2}^3 e^{3\iota K_2 \tau} + \phi_{\theta_2}^2\phi_{\theta_2}^* e^{\iota K_2 \tau} - \phi_{\theta_2}\phi_{\theta_2}^{*2} e^{-\iota K_2 \tau} - \phi_{\theta_2}^{*3} e^{-3\iota K_2 \tau}\Big)\Bigg].
\end{aligned}
\tag{A.7}
$$

Dividing Eq. (A.7) by $e^{\iota K_2 \tau}$ gives the evolution equation of the complex envelope:

$$
\begin{aligned}
&\dot{\phi}_{y_2} + \iota K_2 \phi_{y_2} - \frac{\iota K_2}{2}\left(\phi_{y_2} + \phi_{y_2}^* e^{-2\iota K_2 \tau}\right) + \xi_{y_2} K_{y_2}\left(\phi_{y_2} + \phi_{y_2}^* e^{-2\iota K_2 \tau}\right) - \frac{\iota K_{y_2}^2}{2K_2}\left(\phi_{y_2} - \phi_{y_2}^* e^{-2\iota K_2 \tau}\right) \\
&= \frac{m_{y_2}^*}{\phi_{y_2 y_2}}\Bigg[\frac{\phi_{y_2 y_2} K_2 H_1^*(K_2)}{2}\left(\phi_{y_2} + \phi_{y_2}^* e^{-2\iota K_2 \tau}\right) + \frac{\phi_{y_2 \theta_2} K_2 H_2^*(K_2)}{2}\left(\phi_{\theta_2} + \phi_{\theta_2}^* e^{-2\iota K_2 \tau}\right) - \frac{\iota \phi_{y_2 \theta_2} K_2 H_3^*(K_2)}{2}\left(\phi_{\theta_2} - \phi_{\theta_2}^* e^{-2\iota K_2 \tau}\right) \\
&\quad - \frac{\iota \phi_{y_2 y_2} K_2 H_4^*(K_2)}{2}\left(\phi_{y_2} - \phi_{y_2}^* e^{-2\iota K_2 \tau}\right) - \frac{\iota K_2}{4}\phi_{\theta_1^2 y_2} b_1^{(2)}\left(\phi_{\theta_1}^2 e^{\iota(2K_1-K_2)\tau} - \phi_{\theta_1}^{*2} e^{-\iota(2K_1+K_2)\tau}\right) - \frac{\iota K_2}{4}\phi_{\theta_2^2 y_2} b_1^{(2)}\left(\phi_{\theta_2}^2 e^{\iota K_2 \tau} - \phi_{\theta_2}^{*2} e^{-3\iota K_2 \tau}\right) \\
&\quad - \frac{\iota K_2}{8}\phi_{\theta_1^2 \theta_2 y_2} b_2^{(2)}\Big(\phi_{\theta_1}^2 \phi_{\theta_2} e^{2\iota K_1 \tau} + 2\phi_{\theta_1}\phi_{\theta_1}^*\phi_{\theta_2} + \phi_{\theta_1}^{*2}\phi_{\theta_2} e^{-2\iota K_1 \tau} - \phi_{\theta_1}^2\phi_{\theta_2}^* e^{2\iota(K_1-K_2)\tau} - 2\phi_{\theta_1}\phi_{\theta_1}^*\phi_{\theta_2}^* e^{-2\iota K_2 \tau} - \phi_{\theta_1}^{*2}\phi_{\theta_2}^* e^{-2\iota(K_1+K_2)\tau}\Big) \\
&\quad - \frac{\iota K_2}{4}\phi_{\theta_1^2 \theta_2 y_2} b_2^{(2)}\Big(\phi_{\theta_1}^2 \phi_{\theta_2} e^{2\iota K_1 \tau} + \phi_{\theta_1}^2\phi_{\theta_2}^* e^{2\iota(K_1-K_2)\tau} - \phi_{\theta_1}^{*2}\phi_{\theta_2} e^{-2\iota K_1 \tau} - \phi_{\theta_1}^{*2}\phi_{\theta_2}^* e^{-2\iota(K_1+K_2)\tau}\Big) \\
&\quad - \frac{\iota K_2}{8}\phi_{\theta_2^3 y_2} b_2^{(2)}\Big(\phi_{\theta_2}^3 e^{2\iota K_2 \tau} + \phi_{\theta_2}^2\phi_{\theta_2}^* - \phi_{\theta_2}\phi_{\theta_2}^{*2} e^{-2\iota K_2 \tau} - \phi_{\theta_2}^{*3} e^{-4\iota K_2 \tau}\Big)\Bigg].
\end{aligned}
\tag{A.8}
$$

Under the same near-1:1 assumption, $K_1 - K_2 = \mathcal{O}(\epsilon)$, the time-independent terms and the frequency-difference modulation $e^{2\iota(K_1-K_2)\tau}$ are retained. By averaging out the other oscillatory terms in Eq. (A.8), the symmetric vertical response is obtained as

$$
\begin{aligned}
\dot{\phi}_{y_2} + \xi_{y_2} K_{y_2} \phi_{y_2} - \frac{\iota\left(K_{y_2}^2 - K_2^2\right)}{2K_2}\phi_{y_2} = \frac{m_{y_2}^*}{\phi_{y_2 y_2}}\Bigg[&\frac{\phi_{y_2 y_2} K_2}{2}\left(H_1^*(K_2) - \iota H_4^*(K_2)\right)\phi_{y_2} + \frac{\phi_{y_2 \theta_2} K_2}{2}\left(H_2^*(K_2) - \iota H_3^*(K_2)\right)\phi_{\theta_2} \\
&- \frac{\iota K_2}{8}\phi_{\theta_2^3 y_2} b_2^{(2)}\phi_{\theta_2}^2\phi_{\theta_2}^* - \frac{\iota K_2}{8}\phi_{\theta_1^2 \theta_2 y_2} b_2^{(2)}\Big(2\phi_{\theta_1}\phi_{\theta_1}^*\phi_{\theta_2} + \phi_{\theta_1}^2\phi_{\theta_2}^* e^{2\iota(K_1-K_2)\tau}\Big)\Bigg].
\end{aligned}
\tag{A.9}
$$

The same procedure is applied to the antisymmetric torsional response. By substituting Eq. (18) into Eq. (17c), the complex response equation becomes

$$
\begin{aligned}
&\dot{\psi}_{\theta_1} - \iota K_1 \frac{\psi_{\theta_1} + \psi_{\theta_1}^*}{2} + 2\xi_{\theta_1} K_{\theta_1}\frac{\psi_{\theta_1} + \psi_{\theta_1}^*}{2} + K_{\theta_1}^2 \frac{\psi_{\theta_1} - \psi_{\theta_1}^*}{2\iota K_1} = \frac{m_{\theta_1}^*}{\phi_{\theta_1 \theta_1}}\Bigg[\phi_{y_1 \theta_1} K_1 A_1^*(K_1)\frac{\psi_{y_1} + \psi_{y_1}^*}{2} + \phi_{\theta_1 \theta_1} K_1 A_2^*(K_1)\frac{\psi_{\theta_1} + \psi_{\theta_1}^*}{2} \\
&\quad + \phi_{\theta_1 \theta_1} K_1^2 A_3^*(K_1)\frac{\psi_{\theta_1} - \psi_{\theta_1}^*}{2\iota K_1} + \phi_{y_1 \theta_1} K_1^2 A_4^*(K_1)\frac{\psi_{y_1} - \psi_{y_1}^*}{2\iota K_1} + 2\phi_{\theta_1^2 \theta_2} c_1^{(1)} K_1 \frac{\psi_{\theta_1} + \psi_{\theta_1}^*}{2}\frac{\psi_{\theta_2} + \psi_{\theta_2}^*}{2} \\
&\quad + 2\phi_{\theta_1^2 \theta_2} c_2^{(1)} K_1^2 K_2 \frac{\psi_{\theta_1} - \psi_{\theta_1}^*}{2\iota K_1}\frac{\psi_{\theta_2} - \psi_{\theta_2}^*}{2\iota K_2} + \phi_{\theta_1^4} c_3^{(1)} K_1 \left(\frac{\psi_{\theta_1} + \psi_{\theta_1}^*}{2}\right)^3 + 3\phi_{\theta_1^2 \theta_2^2} c_3^{(1)} K_1 \frac{\psi_{\theta_1} + \psi_{\theta_1}^*}{2}\left(\frac{\psi_{\theta_2} + \psi_{\theta_2}^*}{2}\right)^2\Bigg].
\end{aligned}
\tag{A.10}
$$

For constant K_1, the derivative in Eq. (A.10) becomes $\dot{\psi}_{\theta_1} = \left(\dot{\phi}_{\theta_1} + \iota K_1 \phi_{\theta_1}\right) e^{\iota K_1 \tau}$. Substitution into Eq. (A.10) gives

$$
\begin{aligned}
&\left(\dot{\phi}_{\theta_1} + \iota K_1 \phi_{\theta_1}\right) e^{\iota K_1 \tau} - \frac{\iota K_1}{2}\left(\phi_{\theta_1} e^{\iota K_1 \tau} + \phi^*_{\theta_1} e^{-\iota K_1 \tau}\right) + \xi_{\theta_1} K_{\theta_1}\left(\phi_{\theta_1} e^{\iota K_1 \tau} + \phi^*_{\theta_1} e^{-\iota K_1 \tau}\right) - \frac{\iota K_{\theta_1}^2}{2K_1}\left(\phi_{\theta_1} e^{\iota K_1 \tau} - \phi^*_{\theta_1} e^{-\iota K_1 \tau}\right) \\
&= \frac{m^*_{\theta_1}}{\phi_{\theta_1\theta_1}}\Bigg[\frac{\phi_{y_1\theta_1} K_1 A_1^*(K_1)}{2}\left(\phi_{y_1} e^{\iota K_1 \tau} + \phi^*_{y_1} e^{-\iota K_1 \tau}\right) + \frac{\phi_{\theta_1\theta_1} K_1 A_2^*(K_1)}{2}\left(\phi_{\theta_1} e^{\iota K_1 \tau} + \phi^*_{\theta_1} e^{-\iota K_1 \tau}\right) - \frac{\iota\phi_{\theta_1\theta_1} K_1 A_3^*(K_1)}{2}\left(\phi_{\theta_1} e^{\iota K_1 \tau} - \phi^*_{\theta_1} e^{-\iota K_1 \tau}\right) \\
&- \frac{\iota\phi_{y_1\theta_1} K_1 A_4^*(K_1)}{2}\left(\phi_{y_1} e^{\iota K_1 \tau} - \phi^*_{y_1} e^{-\iota K_1 \tau}\right) + \frac{K_1}{2}\phi_{\theta_1^2\theta_2} c_1^{(1)}\Big(\phi_{\theta_1}\phi_{\theta_2} e^{\iota(K_1+K_2)\tau} + \phi_{\theta_1}\phi^*_{\theta_2} e^{\iota(K_1-K_2)\tau} + \phi^*_{\theta_1}\phi_{\theta_2} e^{\iota(K_2-K_1)\tau} + \phi^*_{\theta_1}\phi^*_{\theta_2} e^{-\iota(K_1+K_2)\tau}\Big) \\
&- \frac{K_1}{2}\phi_{\theta_1^2\theta_2} c_2^{(1)}\Big(\phi_{\theta_1}\phi_{\theta_2} e^{\iota(K_1+K_2)\tau} - \phi_{\theta_1}\phi^*_{\theta_2} e^{\iota(K_1-K_2)\tau} - \phi^*_{\theta_1}\phi_{\theta_2} e^{\iota(K_2-K_1)\tau} + \phi^*_{\theta_1}\phi^*_{\theta_2} e^{-\iota(K_1+K_2)\tau}\Big) \\
&+ \frac{K_1}{8}\phi_{\theta_1^4} c_3^{(1)}\Big(\phi^3_{\theta_1} e^{3\iota K_1 \tau} + 3\phi^2_{\theta_1}\phi^*_{\theta_1} e^{\iota K_1 \tau} + 3\phi_{\theta_1}\phi^{*2}_{\theta_1} e^{-\iota K_1 \tau} + \phi^{*3}_{\theta_1} e^{-3\iota K_1 \tau}\Big) \\
&+ \frac{3K_1}{8}\phi_{\theta_1^2\theta_2^2} c_3^{(1)}\Big(\phi_{\theta_1}\phi^2_{\theta_2} e^{\iota(K_1+2K_2)\tau} + 2\phi_{\theta_1}\phi_{\theta_2}\phi^*_{\theta_2} e^{\iota K_1 \tau} + \phi_{\theta_1}\phi^{*2}_{\theta_2} e^{\iota(K_1-2K_2)\tau} + \phi^*_{\theta_1}\phi^2_{\theta_2} e^{\iota(2K_2-K_1)\tau} + 2\phi^*_{\theta_1}\phi_{\theta_2}\phi^*_{\theta_2} e^{-\iota K_1 \tau} + \phi^*_{\theta_1}\phi^{*2}_{\theta_2} e^{-\iota(K_1+2K_2)\tau}\Big)\Bigg].
\end{aligned}
\tag{A.11}
$$

Dividing Eq. (A.11) by $e^{\iota K_1 \tau}$ gives the evolution equation of the complex envelope:

$$
\begin{aligned}
&\dot{\phi}_{\theta_1} + \iota K_1 \phi_{\theta_1} - \frac{\iota K_1}{2}\left(\phi_{\theta_1} + \phi^*_{\theta_1} e^{-2\iota K_1 \tau}\right) + \xi_{\theta_1} K_{\theta_1}\left(\phi_{\theta_1} + \phi^*_{\theta_1} e^{-2\iota K_1 \tau}\right) - \frac{\iota K_{\theta_1}^2}{2K_1}\left(\phi_{\theta_1} - \phi^*_{\theta_1} e^{-2\iota K_1 \tau}\right) \\
&= \frac{m^*_{\theta_1}}{\phi_{\theta_1\theta_1}}\Bigg[\frac{\phi_{y_1\theta_1} K_1 A_1^*(K_1)}{2}\left(\phi_{y_1} + \phi^*_{y_1} e^{-2\iota K_1 \tau}\right) + \frac{\phi_{\theta_1\theta_1} K_1 A_2^*(K_1)}{2}\left(\phi_{\theta_1} + \phi^*_{\theta_1} e^{-2\iota K_1 \tau}\right) - \frac{\iota\phi_{\theta_1\theta_1} K_1 A_3^*(K_1)}{2}\left(\phi_{\theta_1} - \phi^*_{\theta_1} e^{-2\iota K_1 \tau}\right) \\
&- \frac{\iota\phi_{y_1\theta_1} K_1 A_4^*(K_1)}{2}\left(\phi_{y_1} - \phi^*_{y_1} e^{-2\iota K_1 \tau}\right) + \frac{K_1}{2}\phi_{\theta_1^2\theta_2} c_1^{(1)}\Big(\phi_{\theta_1}\phi_{\theta_2} e^{\iota K_2 \tau} + \phi_{\theta_1}\phi^*_{\theta_2} e^{-\iota K_2 \tau} + \phi^*_{\theta_1}\phi_{\theta_2} e^{\iota(K_2-2K_1)\tau} + \phi^*_{\theta_1}\phi^*_{\theta_2} e^{-\iota(2K_1+K_2)\tau}\Big) \\
&- \frac{K_1}{2}\phi_{\theta_1^2\theta_2} c_2^{(1)}\Big(\phi_{\theta_1}\phi_{\theta_2} e^{\iota K_2 \tau} - \phi_{\theta_1}\phi^*_{\theta_2} e^{-\iota K_2 \tau} - \phi^*_{\theta_1}\phi_{\theta_2} e^{\iota(K_2-2K_1)\tau} + \phi^*_{\theta_1}\phi^*_{\theta_2} e^{-\iota(2K_1+K_2)\tau}\Big) \\
&+ \frac{K_1}{8}\phi_{\theta_1^4} c_3^{(1)}\Big(\phi^3_{\theta_1} e^{2\iota K_1 \tau} + 3\phi^2_{\theta_1}\phi^*_{\theta_1} + 3\phi_{\theta_1}\phi^{*2}_{\theta_1} e^{-2\iota K_1 \tau} + \phi^{*3}_{\theta_1} e^{-4\iota K_1 \tau}\Big) \\
&+ \frac{3K_1}{8}\phi_{\theta_1^2\theta_2^2} c_3^{(1)}\Big(\phi_{\theta_1}\phi^2_{\theta_2} e^{2\iota K_2 \tau} + 2\phi_{\theta_1}\phi_{\theta_2}\phi^*_{\theta_2} + \phi_{\theta_1}\phi^{*2}_{\theta_2} e^{-2\iota K_2 \tau} + \phi^*_{\theta_1}\phi^2_{\theta_2} e^{2\iota(K_2-K_1)\tau} + 2\phi^*_{\theta_1}\phi_{\theta_2}\phi^*_{\theta_2} e^{-2\iota K_1 \tau} + \phi^*_{\theta_1}\phi^{*2}_{\theta_2} e^{-2\iota(K_1+K_2)\tau}\Big)\Bigg].
\end{aligned}
\tag{A.12}
$$

Under the same near-1 : 1 assumption, $K_2 - K_1 = \mathcal{O}(\epsilon)$, the time-independent terms and the frequency-difference modulation $e^{2\iota(K_2-K_1)\tau}$ are retained. By averaging out the other oscillatory terms in Eq. (A.12), the antisymmetric torsional response is obtained as

$$
\begin{aligned}
\dot{\phi}_{\theta_1} + \xi_{\theta_1} K_{\theta_1}\phi_{\theta_1} - \frac{\iota\left(K_{\theta_1}^2 - K_1^2\right)}{2K_1}\phi_{\theta_1} = \frac{m^*_{\theta_1}}{\phi_{\theta_1\theta_1}}\Bigg[&\frac{\phi_{y_1\theta_1} K_1}{2}\left(A_1^*(K_1) - \iota A_4^*(K_1)\right)\phi_{y_1} + \frac{\phi_{\theta_1\theta_1} K_1}{2}\left(A_2^*(K_1) - \iota A_3^*(K_1)\right)\phi_{\theta_1} \\
&+ \frac{3K_1}{8}\phi_{\theta_1^4} c_3^{(1)}\phi^2_{\theta_1}\phi^*_{\theta_1} + \frac{3K_1}{8}\phi_{\theta_1^2\theta_2^2} c_3^{(1)}\Big(2\phi_{\theta_1}\phi_{\theta_2}\phi^*_{\theta_2} + \phi^*_{\theta_1}\phi^2_{\theta_2} e^{2\iota(K_2-K_1)\tau}\Big)\Bigg].
\end{aligned}
\tag{A.13}
$$

For the symmetric torsional response, substituting Eq. (18) into Eq. (17d) gives

$$
\begin{aligned}
&\dot{\psi}_{\theta_2} - \iota K_2 \frac{\psi_{\theta_2} + \psi^*_{\theta_2}}{2} + 2\xi_{\theta_2} K_{\theta_2}\frac{\psi_{\theta_2} + \psi^*_{\theta_2}}{2} + K_{\theta_2}^2 \frac{\psi_{\theta_2} - \psi^*_{\theta_2}}{2\iota K_2} = \frac{m^*_{\theta_2}}{\phi_{\theta_2\theta_2}}\Bigg[\phi_{y_2\theta_2} K_2 A_1^*(K_2)\frac{\psi_{y_2} + \psi^*_{y_2}}{2} + \phi_{\theta_2\theta_2} K_2 A_2^*(K_2)\frac{\psi_{\theta_2} + \psi^*_{\theta_2}}{2} \\
&+ \phi_{\theta_2\theta_2} K_2^2 A_3^*(K_2)\frac{\psi_{\theta_2} - \psi^*_{\theta_2}}{2\iota K_2} + \phi_{y_2\theta_2} K_2^2 A_4^*(K_2)\frac{\psi_{y_2} - \psi^*_{y_2}}{2\iota K_2} + \phi_{\theta_1^2\theta_2} c_1^{(2)} K_2\left(\frac{\psi_{\theta_1} + \psi^*_{\theta_1}}{2}\right)^2 + \phi_{\theta_2^3} c_1^{(2)} K_2\left(\frac{\psi_{\theta_2} + \psi^*_{\theta_2}}{2}\right)^2 \\
&+ \phi_{\theta_1^2\theta_2} c_2^{(2)} K_1^2 K_2\left(\frac{\psi_{\theta_1} - \psi^*_{\theta_1}}{2\iota K_1}\right)^2 + \phi_{\theta_2^3} c_2^{(2)} K_2^3\left(\frac{\psi_{\theta_2} - \psi^*_{\theta_2}}{2\iota K_2}\right)^2 + 3\phi_{\theta_1^2\theta_2^2} c_3^{(2)} K_2\left(\frac{\psi_{\theta_1} + \psi^*_{\theta_1}}{2}\right)^2\frac{\psi_{\theta_2} + \psi^*_{\theta_2}}{2} + \phi_{\theta_2^4} c_3^{(2)} K_2\left(\frac{\psi_{\theta_2} + \psi^*_{\theta_2}}{2}\right)^3\Bigg].
\end{aligned}
\tag{A.14}
$$

For constant K_2, the derivative in Eq. (A.14) becomes $\dot{\psi}_{\theta_2} = \left(\dot{\phi}_{\theta_2} + \iota K_2 \phi_{\theta_2}\right) e^{\iota K_2 \tau}$. Substitution into Eq. (A.14) gives

$$
\begin{aligned}
&\left(\dot{\phi}_{\theta_2} + \iota K_2 \phi_{\theta_2}\right) e^{\iota K_2 \tau} - \frac{\iota K_2}{2}\left(\phi_{\theta_2} e^{\iota K_2 \tau} + \phi^*_{\theta_2} e^{-\iota K_2 \tau}\right) + \xi_{\theta_2} K_{\theta_2}\left(\phi_{\theta_2} e^{\iota K_2 \tau} + \phi^*_{\theta_2} e^{-\iota K_2 \tau}\right) - \frac{\iota K_{\theta_2}^2}{2K_2}\left(\phi_{\theta_2} e^{\iota K_2 \tau} - \phi^*_{\theta_2} e^{-\iota K_2 \tau}\right) \\
&= \frac{m^*_{\theta_2}}{\phi_{\theta_2\theta_2}}\Bigg[\frac{\phi_{y_2\theta_2} K_2 A_1^*(K_2)}{2}\left(\phi_{y_2} e^{\iota K_2 \tau} + \phi^*_{y_2} e^{-\iota K_2 \tau}\right) + \frac{\phi_{\theta_2\theta_2} K_2 A_2^*(K_2)}{2}\left(\phi_{\theta_2} e^{\iota K_2 \tau} + \phi^*_{\theta_2} e^{-\iota K_2 \tau}\right) - \frac{\iota \phi_{\theta_2\theta_2} K_2 A_3^*(K_2)}{2}\left(\phi_{\theta_2} e^{\iota K_2 \tau} - \phi^*_{\theta_2} e^{-\iota K_2 \tau}\right) \\
&- \frac{\iota \phi_{y_2\theta_2} K_2 A_4^*(K_2)}{2}\left(\phi_{y_2} e^{\iota K_2 \tau} - \phi^*_{y_2} e^{-\iota K_2 \tau}\right) + \frac{K_2}{4}\phi_{\theta_1^2\theta_2} c_1^{(2)}\left(\phi^2_{\theta_1} e^{2\iota K_1 \tau} + 2\phi_{\theta_1}\phi^*_{\theta_1} + \phi^{*2}_{\theta_1} e^{-2\iota K_1 \tau}\right) + \frac{K_2}{4}\phi_{\theta_2^3} c_1^{(2)}\left(\phi^2_{\theta_2} e^{2\iota K_2 \tau} + 2\phi_{\theta_2}\phi^*_{\theta_2} + \phi^{*2}_{\theta_2} e^{-2\iota K_2 \tau}\right) \\
&- \frac{K_2}{4}\phi_{\theta_1^2\theta_2} c_2^{(2)}\left(\phi^2_{\theta_1} e^{2\iota K_1 \tau} - 2\phi_{\theta_1}\phi^*_{\theta_1} + \phi^{*2}_{\theta_1} e^{-2\iota K_1 \tau}\right) - \frac{K_2}{4}\phi_{\theta_2^3} c_2^{(2)}\left(\phi^2_{\theta_2} e^{2\iota K_2 \tau} - 2\phi_{\theta_2}\phi^*_{\theta_2} + \phi^{*2}_{\theta_2} e^{-2\iota K_2 \tau}\right) \\
&+ \frac{3K_2}{8}\phi_{\theta_1^2\theta_2^2} c_3^{(2)}\left(\phi^2_{\theta_1}\phi_{\theta_2} e^{\iota(2K_1+K_2)\tau} + \phi^2_{\theta_1}\phi^*_{\theta_2} e^{\iota(2K_1-K_2)\tau} + 2\phi_{\theta_1}\phi^*_{\theta_1}\phi_{\theta_2} e^{\iota K_2 \tau} + 2\phi_{\theta_1}\phi^*_{\theta_1}\phi^*_{\theta_2} e^{-\iota K_2 \tau} + \phi^{*2}_{\theta_1}\phi_{\theta_2} e^{\iota(K_2-2K_1)\tau} + \phi^{*2}_{\theta_1}\phi^*_{\theta_2} e^{-\iota(2K_1+K_2)\tau}\right) \\
&+ \frac{K_2}{8}\phi_{\theta_2^4} c_3^{(2)}\left(\phi^3_{\theta_2} e^{3\iota K_2 \tau} + 3\phi^2_{\theta_2}\phi^*_{\theta_2} e^{\iota K_2 \tau} + 3\phi_{\theta_2}\phi^{*2}_{\theta_2} e^{-\iota K_2 \tau} + \phi^{*3}_{\theta_2} e^{-3\iota K_2 \tau}\right)\Bigg].
\end{aligned}
\tag{A.15}
$$

Dividing Eq. (A.15) by $e^{\iota K_2 \tau}$ gives the evolution equation of the complex envelope:

$$
\begin{aligned}
&\dot{\phi}_{\theta_2} + \iota K_2 \phi_{\theta_2} - \frac{\iota K_2}{2}\left(\phi_{\theta_2} + \phi^*_{\theta_2} e^{-2\iota K_2 \tau}\right) + \xi_{\theta_2} K_{\theta_2}\left(\phi_{\theta_2} + \phi^*_{\theta_2} e^{-2\iota K_2 \tau}\right) - \frac{\iota K_{\theta_2}^2}{2K_2}\left(\phi_{\theta_2} - \phi^*_{\theta_2} e^{-2\iota K_2 \tau}\right) \\
&= \frac{m^*_{\theta_2}}{\phi_{\theta_2\theta_2}}\Bigg[\frac{\phi_{y_2\theta_2} K_2 A_1^*(K_2)}{2}\left(\phi_{y_2} + \phi^*_{y_2} e^{-2\iota K_2 \tau}\right) + \frac{\phi_{\theta_2\theta_2} K_2 A_2^*(K_2)}{2}\left(\phi_{\theta_2} + \phi^*_{\theta_2} e^{-2\iota K_2 \tau}\right) - \frac{\iota \phi_{\theta_2\theta_2} K_2 A_3^*(K_2)}{2}\left(\phi_{\theta_2} - \phi^*_{\theta_2} e^{-2\iota K_2 \tau}\right) \\
&- \frac{\iota \phi_{y_2\theta_2} K_2 A_4^*(K_2)}{2}\left(\phi_{y_2} - \phi^*_{y_2} e^{-2\iota K_2 \tau}\right) + \frac{K_2}{4}\phi_{\theta_1^2\theta_2} c_1^{(2)}\left(\phi^2_{\theta_1} e^{\iota(2K_1-K_2)\tau} + 2\phi_{\theta_1}\phi^*_{\theta_1} e^{-\iota K_2 \tau} + \phi^{*2}_{\theta_1} e^{-\iota(2K_1+K_2)\tau}\right) + \frac{K_2}{4}\phi_{\theta_2^3} c_1^{(2)}\left(\phi^2_{\theta_2} e^{\iota K_2 \tau} + 2\phi_{\theta_2}\phi^*_{\theta_2} e^{-\iota K_2 \tau} + \phi^{*2}_{\theta_2} e^{-3\iota K_2 \tau}\right) \\
&- \frac{K_2}{4}\phi_{\theta_1^2\theta_2} c_2^{(2)}\left(\phi^2_{\theta_1} e^{\iota(2K_1-K_2)\tau} - 2\phi_{\theta_1}\phi^*_{\theta_1} e^{-\iota K_2 \tau} + \phi^{*2}_{\theta_1} e^{-\iota(2K_1+K_2)\tau}\right) - \frac{K_2}{4}\phi_{\theta_2^3} c_2^{(2)}\left(\phi^2_{\theta_2} e^{\iota K_2 \tau} - 2\phi_{\theta_2}\phi^*_{\theta_2} e^{-\iota K_2 \tau} + \phi^{*2}_{\theta_2} e^{-3\iota K_2 \tau}\right) \\
&+ \frac{3K_2}{8}\phi_{\theta_1^2\theta_2^2} c_3^{(2)}\left(\phi^2_{\theta_1}\phi_{\theta_2} e^{2\iota K_1 \tau} + \phi^2_{\theta_1}\phi^*_{\theta_2} e^{2\iota(K_1-K_2)\tau} + 2\phi_{\theta_1}\phi^*_{\theta_1}\phi_{\theta_2} + 2\phi_{\theta_1}\phi^*_{\theta_1}\phi^*_{\theta_2} e^{-2\iota K_2 \tau} + \phi^{*2}_{\theta_1}\phi_{\theta_2} e^{-2\iota K_1 \tau} + \phi^{*2}_{\theta_1}\phi^*_{\theta_2} e^{-2\iota(K_1+K_2)\tau}\right) \\
&+ \frac{K_2}{8}\phi_{\theta_2^4} c_3^{(2)}\left(\phi^3_{\theta_2} e^{2\iota K_2 \tau} + 3\phi^2_{\theta_2}\phi^*_{\theta_2} + 3\phi_{\theta_2}\phi^{*2}_{\theta_2} e^{-2\iota K_2 \tau} + \phi^{*3}_{\theta_2} e^{-4\iota K_2 \tau}\right)\Bigg].
\end{aligned}
\tag{A.16}
$$

Under the same near-1:1 assumption, $K_1 - K_2 = \mathcal{O}(\epsilon)$, the time-independent terms and the frequency-difference modulation $e^{2\iota(K_1-K_2)\tau}$ are retained. By averaging out the other oscillatory terms in Eq. (A.16), the symmetric torsional response is obtained as

$$
\begin{aligned}
\dot{\phi}_{\theta_2} + \xi_{\theta_2} K_{\theta_2} \phi_{\theta_2} - \frac{\iota\left(K_{\theta_2}^2 - K_2^2\right)}{2K_2}\phi_{\theta_2} = \frac{m^*_{\theta_2}}{\phi_{\theta_2\theta_2}}\Bigg[&\frac{\phi_{y_2\theta_2} K_2}{2}\left(A_1^*(K_2) - \iota A_4^*(K_2)\right)\phi_{y_2} + \frac{\phi_{\theta_2\theta_2} K_2}{2}\left(A_2^*(K_2) - \iota A_3^*(K_2)\right)\phi_{\theta_2} \\
&+ \frac{3K_2}{8}\phi_{\theta_1^2\theta_2^2} c_3^{(2)}\left(2\phi_{\theta_1}\phi^*_{\theta_1}\phi_{\theta_2} + \phi^2_{\theta_1}\phi^*_{\theta_2} e^{2\iota(K_1-K_2)\tau}\right) + \frac{3K_2}{8}\phi_{\theta_2^4} c_3^{(2)}\phi^2_{\theta_2}\phi^*_{\theta_2}\Bigg].
\end{aligned}
\tag{A.17}
$$

B Comparison of aerodynamic frequency assignments

The two frequency assignments differ in how the displacement contributions are weighted. In the adopted source-frequency weighting, Eq. (14), each contribution q_j is weighted by its own reduced frequency K_j. The alternative receiving-frequency weighting replaces $\mathcal{K}[q]$ by $K_r(q_1 + q_2)$. Both assignments use the receiving branch frequency K_r for the leading factor and aerodynamic coefficients and retain the exact velocity $\dot{q}$. The superscripts src and rec denote source-frequency weighting and receiving-frequency weighting, respectively. For the other branch $s \neq r$, define the load differences as $\Delta\hat{n}_{L,r} = \hat{n}^{\mathrm{src}}_{L,r} - \hat{n}^{\mathrm{rec}}_{L,r}$ and $\Delta\hat{n}_{M,r} = \hat{n}^{\mathrm{src}}_{M,r} - \hat{n}^{\mathrm{rec}}_{M,r}$. By subtracting the two force expressions, the differences are obtained as

$$\Delta\hat{n}_{L,r} = K_r(K_s - K_r)q_s \left[b_1^{(r)}\dot{q} + b_2^{(r)}(\dot{q})^2 \right], \tag{B.1a}$$

$$\Delta\hat{n}_{M,r} = K_r c_2^{(r)} \left[2K_r(K_s - K_r)q_r q_s + (K_s^2 - K_r^2)q_s^2 \right]. \tag{B.1b}$$

The terms involving $c_1^{(r)}$ and $c_3^{(r)}$ are identical for the two rules. The remaining differences vanish when $K_1 = K_2$, but generally remain in the original equations when the two frequencies differ.

By applying the stated modal symmetry to Eq. (B.1), the surviving cubic lift difference is proportional to $\theta_s\dot{\theta}_s\dot{\theta}_r$. For the harmonic carrier, $\theta_s\dot{\theta}_s$ has no constant component, and this product gives no time-independent resonant contribution. The quadratic force differences also give no fundamental resonant contribution in the leading-order near-1 : 1 averaging used here. Therefore, the two frequency assignments give the same autonomous secular subsystem under these assumptions.

For $\xi_{\mathrm{nl}} = 120$, continuation calculations using either frequency assignment on the 90–100 m/s grid give identical equilibrium amplitudes and transverse stability eigenvalues. This agreement follows from the identical secular equations and does not establish equivalence of the original equations or the complete averaged response histories.

The cubic lift difference does contribute to the frequency-difference modulation retained in the complete averaged equations. With the same subtraction order, the difference in the vertical envelope derivative, evaluated at the same envelope state, is denoted by $\Delta\dot{\phi}_{y_r}$. Complexification gives

$$\begin{aligned}\Delta\dot{\phi}_{y_r} = &-\iota\frac{m^*_{y_r}}{\phi_{y_r y_r}}\frac{K_r(K_s-K_r)}{4K_s}b_2^{(r)}\phi_{\theta_r\theta_s^2 y_r}\\ &\times\phi_{\theta_s}^2\phi^*_{\theta_r}e^{2\iota(K_s-K_r)\tau}, \qquad s\neq r.\end{aligned} \tag{B.2}$$

The torsional envelope equations are unchanged at this averaging order. According to Eq. (B.2), the coefficient of $\phi^*_{\theta_r}\phi^2_{\theta_s}e^{2\iota(K_s-K_r)\tau}$ in the vertical envelope equation is multiplied by $2K_r/K_s-1$ when source-frequency weighting is replaced by receiving-frequency weighting.

At $U = 94$ m/s, the calculated reference frequencies are $K_1 = 0.593460$ and $K_2 = 0.790631$. The beat coefficients for receiving-frequency weighting divided by those for source-frequency weighting are 0.50123 for the antisymmetric vertical equation and 1.66448 for the symmetric vertical equation, corresponding to changes of −49.88% and 66.45%, respectively. Direct Fourier extraction of the mixed cubic lift terms confirms these coefficient ratios. These values describe the change in the beat coefficients; their effect on response amplitudes requires integration with the beat terms retained. Under a strict weak-nonlinearity and near-1 : 1 ordering, the difference between the two frequency assignments is of higher order; the values above use the finite frequency separation of the present model.